



Modeling of dielectric elastomers: Design of actuators and energy harvesting devices



David L. Henann^a, Shawn A. Chester^b, Katia Bertoldi^{a,*}

^a School of Engineering and Applied Sciences, Harvard University, Cambridge, MA 02138, USA

^b Department of Mechanical & Industrial Engineering, New Jersey Institute of Technology, Newark, NJ 07102, USA

ARTICLE INFO

Article history:

Received 11 September 2012

Received in revised form

19 January 2013

Accepted 12 May 2013

Available online 27 May 2013

Keywords:

Dielectric elastomers

Large deformations

Actuators

Energy harvesting devices

Finite-element method

ABSTRACT

Dielectric elastomers undergo large deformations in response to an electric field and consequently have attracted significant interest as electromechanical transducers. Applications of these materials include actuators capable of converting an applied electric field into mechanical motion and energy harvesting devices that convert mechanical energy into electrical energy. Numerically based design tools are needed to facilitate the development and optimization of these devices. In this paper, we report on our modeling capability for dielectric elastomers. We present the governing equations for the electro-mechanically coupled behavior of dielectric elastomers in a thermodynamic framework and discuss the attendant finite-element formulation and implementation, using a commercial finite-element code. We then utilize our simulation capability to design and optimize complex dielectric elastomeric actuators and energy harvesting devices in various settings.

© 2013 Elsevier Ltd. All rights reserved.

1. Introduction

Dielectric elastomers, or soft dielectrics, are rubbery materials that undergo large elastic deformations in response to an applied electric field (cf. e.g. Pelrine et al., 1998; Zhang et al., 1998; Plante and Dubowsky, 2006; Hossain et al., 2012; Tagarielli et al., 2012). These materials were first reported by Pelrine and coworkers (Pelrine et al., 1998, 2000a,b; Kornbluh et al., 2000) and have since then garnered interest as electromechanical transducers for a wide variety of applications (Carpi et al., 2008), such as robotics, biomedical engineering and energy harvesting. Their capacity for large, reversible deformations distinguishes dielectric elastomers from more conventional electromechanical transducers, such as piezoelectrics. Soft dielectrics are also comparatively lighter, more compliant and less expensive, increasing their appeal.

At a microscopic level, dielectric elastomers are electrically insulating, polymeric materials made up of long-chain molecules, possessing charge imbalances that align, or polarize, in the presence of an electric field. Since these materials can achieve both large mechanical deformations and electrically polarize, they are capable of converting energy between mechanical and electrical forms. In particular, actuators that convert an applied electric field into mechanical motion have been used in robotics, including as artificial muscles for biomimetic robots and prosthetics (Bar-Cohen, 2001; Brochu and Pei, 2010; Carpi et al., 2005; Carpi and Smela, 2009). In contrast, soft dielectric devices that convert mechanical energy into electrical energy are referred to as energy harvesting devices (Kornbluh et al., 2011, 2012). In these applications, mechanical energy from motion such as human walking or ocean waves is converted to electrical energy and stored. These technologies

* Corresponding author. Tel.: +1 8572347352.

E-mail address: bertoldi@seas.harvard.edu (K. Bertoldi).

have been demonstrated in practice; however, the development of rigorous design tools that may be used for optimization in varied applications remains a challenge.

A design capability for dielectric elastomers requires (i) a finite-deformation constitutive theory for the electromechanically coupled response of these materials and (ii) a robust numerical implementation of the resulting field equations. Work on electromechanically coupled constitutive theories goes back many decades (Toupin, 1956, 1963; Maugin, 1980, 1988; Eringen and Maugin, 1990; Maugin et al., 1992; Goulbourne et al., 2005; Dorfmann and Ogden, 2005; Bustamante et al., 2009), and in recent years the mechanics community has come to a relative agreement regarding the formulation of a theory in a thermodynamic framework (McMeeking and Landis, 2005; McMeeking et al., 2007; Suo et al., 2008; Zhao et al., 2007; Zhao and Suo, 2008a). However, there remains a need for numerical tools capable of predicting the large-deformation, three-dimensional, coupled response. Several approaches have been undertaken. First, simplified finite-element computational procedures have been proposed that make geometrical assumptions, reducing the electrical problem to one dimension (Wissler and Mazza, 2005, 2007; Zhao and Suo, 2008b; Zhou et al., 2008). These techniques are useful for basic actuator configurations; however, fully three-dimensional procedures are needed to guide the design of more complex devices. Recently, finite-element implementations have been reported using in-house codes both in quasi-static (Vu and Steinmann, 2007; Vu et al., 2007) and dynamic settings (Park et al., 2012); however, these codes are not available to the community. Given the industrial and scientific community's growing interest in dielectric elastomers, implementation of the theory within a widely available finite-element software is a crucial step toward facilitating interactions between industry and researchers and guiding the design of complex three-dimensional devices. Unfortunately, this task is not straightforward within commercial finite-element packages, since additional nodal degrees of freedom are required. Few efforts in this direction have been reported, namely using FEAP (Gao et al., 2011) and Comsol (Rudykh and deBotton, 2012). However, since FEAP is a general-purpose finite-element program, designed for research and educational use, it is not available to the industrial community. Moreover, although Comsol is amenable to the implementation of the coupled electromechanical theory, its difficulty in dealing with large deformations is well-known, and as such, it is not well-suited for problems involving dielectric elastomers.

To overcome these issues, the purpose of this paper is threefold: (i) to present a concise thermodynamic development of the three-dimensional, fully coupled theory governing the behavior of dielectric elastomers, (ii) to implement the theory in the commercial finite-element code *Abaqus/Standard* (2010), taking full advantage of the capability to actively interact with the software through user-defined subroutines, and (iii) to utilize the code to provide new insights, through simulation, into the design and optimization of complex actuators and energy harvesting devices in various settings. *Abaqus* is an attractive platform because it is a well-known code, widely available, stable, portable, and particularly suitable for analyses involving large deformations. The novelty of the present work is in its completeness, encompassing theoretical formulation, numerical implementation, and application to design and optimization. We expect our simulations of actuators and energy harvesting devices to aid in improving upon the designs of these structures. Further, our *Abaqus* user-defined subroutines and input files may be found online as supplementary material to be used and expanded upon by the community in further research on dielectric elastomers.

The paper is organized as follows. In [Section 2](#), we lay out the continuum framework used to address the electromechanical behavior, and in [Section 3](#), we specify specific constitutive equations for a representative dielectric elastomer. In [Section 4](#), we review the resulting boundary-value problem and its finite-element implementation. Finally, in [Section 5](#), we verify our finite-element implementation and demonstrate its application by simulating the operation of several complex actuators and energy harvesting devices made from dielectric elastomers.

2. Continuum framework

In this section, we summarize the equations governing the nonlinear, electrostatic deformation of soft dielectrics, following the formulations previously introduced by McMeeking and Suo and their coworkers (McMeeking and Landis, 2005; McMeeking et al., 2007; Suo et al., 2008; Zhao et al., 2007; Zhao and Suo, 2008a).

Kinematics. We consider a homogeneous body \mathcal{B}_R identified with the region of space it occupies in a fixed reference configuration, and denote by \mathbf{x}_R an arbitrary material point of \mathcal{B}_R . A motion of \mathcal{B}_R is then a smooth one-to-one mapping $\mathbf{x} = \chi(\mathbf{x}_R, t)$ with deformation gradient given by¹

$$\mathbf{F} = \nabla \chi, \quad (2.1)$$

such that $J = \det \mathbf{F} > 0$. The right and left and polar decompositions of \mathbf{F} are given by $\mathbf{F} = \mathbf{R}\mathbf{U} = \mathbf{V}\mathbf{R}$, where \mathbf{R} is a rotation (proper orthogonal tensor), while \mathbf{U} and \mathbf{V} are symmetric, positive-definite stretch tensors. Also, the right and left Cauchy-Green tensors are given by $\mathbf{C} = \mathbf{U}^2 = \mathbf{F}^T \mathbf{F}$ and $\mathbf{B} = \mathbf{V}^2 = \mathbf{F} \mathbf{F}^T$, respectively.

Electric potential, electric field and Faraday's law. Central to the discussion of dielectric elastomeric materials is the electric potential $\varphi(\mathbf{x}_R, t)$. We define the referential electric field as

$$\mathbf{E}_R \stackrel{\text{def}}{=} -\nabla \varphi, \quad (2.2)$$

¹ The symbols ∇ , Div and Curl denote the gradient, divergence and curl respectively with respect to the material point \mathbf{x}_R in the reference configuration; grad , div and curl denote these operators with respect to the point $\mathbf{x} = \chi(\mathbf{x}_R, t)$ in the deformed configuration.

so that the referential electric field obeys

$$\text{Curl} \mathbf{E}_R = \mathbf{0}, \quad (2.3)$$

which is the electrostatic form of Faraday's Law.

Likewise, we may define the spatial electric field as

$$\mathbf{E} \stackrel{\text{def}}{=} -\text{grad } \varphi, \quad (2.4)$$

and thus

$$\text{curl} \mathbf{E} = \mathbf{0}. \quad (2.5)$$

We note that the referential and spatial electric fields are related by $\mathbf{E}_R = \mathbf{F}^T \mathbf{E}$.

Equilibrium. Throughout, we denote by \mathcal{P}_R an arbitrary subregion of the reference body \mathcal{B}_R , by \mathbf{n}_R the outward unit normal on its boundary $\partial \mathcal{P}_R$ and by \mathbf{T}_R the standard first Piola stress tensor. Neglecting inertial effects, the balance of forces and moments in \mathcal{P}_R are expressed referentially as

$$\text{Div} \mathbf{T}_R + \mathbf{b}_R = \mathbf{0}, \quad \mathbf{T}_R \mathbf{F}^T = \mathbf{F} \mathbf{T}_R^T, \quad (2.6)$$

respectively, where \mathbf{b}_R is an external body force per unit reference volume. Further, the external surface traction on an element of the surface $\partial \mathcal{P}_R$ is given by

$$\mathbf{t}_R(\mathbf{n}_R) = [[\mathbf{T}_R]] \mathbf{n}_R, \quad (2.7)$$

where $[[\cdot]]$ is the jump operator on the boundary $\partial \mathcal{P}_R$, defined as the difference between the quantity inside and outside the domain, i.e. $[[\mathbf{T}_R]] = \mathbf{T}_R^{\text{in}} - \mathbf{T}_R^{\text{out}}$ on $\partial \mathcal{P}_R$. As is standard, the Piola stress \mathbf{T}_R is related to the standard symmetric Cauchy stress \mathbf{T} in the deformed configuration by $\mathbf{T}_R = \mathbf{J} \mathbf{T} \mathbf{F}^{-T}$. We note that what we call the Cauchy stress here is often referred to as the total stress in the dielectric elastomer literature; however, we see no need to distinguish between a purely mechanical stress and an electrostatic, or Maxwell, stress.

Gauss's law. We introduce the vector field \mathbf{D}_R , which denotes the electric displacement in the reference configuration. Neglecting electrodynamic effects, Gauss's law may be expressed referentially as

$$\text{Div} \mathbf{D}_R = q_R, \quad (2.8)$$

where q_R is the free charge density per unit reference volume. Further, the free charge density on an element of the surface $\partial \mathcal{P}_R$ of \mathcal{P}_R is given by

$$\omega_R(\mathbf{n}_R) = -[[\mathbf{D}_R]] \cdot \mathbf{n}_R, \quad (2.9)$$

where $[[\mathbf{D}_R]] = \mathbf{D}_R^{\text{in}} - \mathbf{D}_R^{\text{out}}$ on $\partial \mathcal{P}_R$. Finally, the referential electric displacement is related to the spatial electric displacement \mathbf{D} in the deformed body by $\mathbf{D}_R = \mathbf{J} \mathbf{F}^{-1} \mathbf{D}$.

Free energy imbalance. We consider a purely electromechanical theory based on a free energy imbalance that represents the first and second laws of thermodynamics under isothermal conditions. This imbalance requires that the temporal increase in the Helmholtz free energy of any subregion be less than or equal to the power expended externally on that subregion. Thus, letting ψ_R denote the Helmholtz free energy measured per unit volume in the reference space, the free energy imbalance takes the form

$$\int_{\mathcal{P}_R} \dot{\psi}_R dv_R \leq \int_{\partial \mathcal{P}_R} \underbrace{[[\mathbf{T}_R]] \mathbf{n}_R}_{\mathbf{t}_R(\mathbf{n}_R)} \cdot \dot{\mathbf{x}} da_R + \int_{\mathcal{P}_R} \mathbf{b}_R \cdot \dot{\mathbf{x}} dv_R + \int_{\partial \mathcal{P}_R} \underbrace{\varphi(-[[\mathbf{D}_R]] \cdot \mathbf{n}_R)}_{\omega_R(\mathbf{n}_R)} da_R + \int_{\mathcal{P}_R} \varphi \dot{q}_R dv_R, \quad (2.10)$$

for each subregion \mathcal{P}_R . In the last two terms, we have adopted the standard notion of external electrical power also employed by McMeeking and Suo and their coworkers (McMeeking and Landis, 2005; McMeeking et al., 2007; Suo et al., 2008; Zhao and Suo, 2008a). Bringing the time derivative inside the integral and using the divergence theorem on the integrals over $\partial \mathcal{P}_R$ reduces (2.10) to

$$\int_{\mathcal{P}_R} \dot{\psi}_R dv_R \leq \int_{\mathcal{P}_R} (\mathbf{T}_R : \dot{\mathbf{F}} + \mathbf{E}_R \cdot \dot{\mathbf{D}}_R) dv_R + \int_{\mathcal{P}_R} (\text{Div} \mathbf{T}_R + \mathbf{b}_R) \cdot \dot{\mathbf{x}} dv_R + \int_{\mathcal{P}_R} \varphi (-\text{Div} \dot{\mathbf{D}}_R + \dot{q}_R) dv_R. \quad (2.11)$$

Using (2.6)₁ and (2.8), and since the subregion \mathcal{P}_R is arbitrary, (2.11) yields the local free energy imbalance

$$\dot{\psi}_R - \mathbf{T}_R : \dot{\mathbf{F}} - \mathbf{E}_R \cdot \dot{\mathbf{D}}_R \leq 0. \quad (2.12)$$

Next, we introduce the second Piola stress

$$\mathbf{S} \stackrel{\text{def}}{=} \mathbf{F}^{-1} \mathbf{T}_R = \mathbf{J} \mathbf{F}^{-1} \mathbf{T} \mathbf{F}^{-T}, \quad (2.13)$$

which is symmetric since \mathbf{T} is symmetric. As is standard the stress power may be expressed in terms of the second Piola stress as

$$\mathbf{T}_R : \dot{\mathbf{F}} = \frac{1}{2} \mathbf{S} : \dot{\mathbf{C}}. \quad (2.14)$$

Use of (2.14) in (2.12) allows us to express the free energy imbalance in an alternate convenient form as

$$\dot{\psi}_R - \frac{1}{2} \mathbf{S} : \dot{\mathbf{C}} - \mathbf{E}_R \cdot \dot{\mathbf{D}}_R \leq 0. \quad (2.15)$$

Finally, we note that since ψ_R is a scalar field, \mathbf{S} and \mathbf{C} are referential tensor fields, and \mathbf{E}_R and \mathbf{D}_R are referential vector fields, the free energy imbalance (2.15) is invariant under a change in frame.

3. Constitutive equations

Guided by the free energy imbalance (2.15), we assume that the free energy ψ_R , the second Piola stress \mathbf{S} and the referential electric field \mathbf{E}_R are given by the following set of constitutive equations:

$$\psi_R = \hat{\psi}_R(\mathbf{C}, \mathbf{D}_R), \quad \mathbf{S} = \hat{\mathbf{S}}(\mathbf{C}, \mathbf{D}_R) \quad \text{and} \quad \mathbf{E}_R = \hat{\mathbf{E}}_R(\mathbf{C}, \mathbf{D}_R). \quad (3.1)$$

Noting from (3.1)₁ that

$$\dot{\psi}_R = \frac{\partial \hat{\psi}_R}{\partial \mathbf{C}} : \dot{\mathbf{C}} + \frac{\partial \hat{\psi}_R}{\partial \mathbf{D}_R} \cdot \dot{\mathbf{D}}_R, \quad (3.2)$$

and substituting (3.2) into (2.15), we find that

$$\left(\frac{\partial \hat{\psi}_R}{\partial \mathbf{C}} - \frac{1}{2} \hat{\mathbf{S}} \right) : \dot{\mathbf{C}} + \left(\frac{\partial \hat{\psi}_R}{\partial \mathbf{D}_R} - \hat{\mathbf{E}}_R \right) \cdot \dot{\mathbf{D}}_R \leq 0. \quad (3.3)$$

This inequality is required to hold for all values of \mathbf{C} and \mathbf{D}_R . Therefore, we are led to the thermodynamic restrictions that the free energy determines the second Piola stress \mathbf{S} and the referential electric field \mathbf{E}_R through the “state relations”

$$\mathbf{S} = 2 \frac{\partial \hat{\psi}_R(\mathbf{C}, \mathbf{D}_R)}{\partial \mathbf{C}} \quad \text{and} \quad \mathbf{E}_R = \frac{\partial \hat{\psi}_R(\mathbf{C}, \mathbf{D}_R)}{\partial \mathbf{D}_R}. \quad (3.4)$$

With a view towards applications, we now specialize the theory by imposing additional constitutive assumptions. Henceforth, we confine our attention to isotropic and nearly incompressible materials.

Isotropic materials. In this case, the response function $\hat{\psi}_R$ must also be isotropic. Thus, $\hat{\psi}_R(\mathbf{C}, \mathbf{D}_R)$ has the representation

$$\hat{\psi}_R(\mathbf{C}, \mathbf{D}_R) = \check{\psi}_R(I_1, I_2, I_3, I_4, I_5, I_6), \quad (3.5)$$

where I_i ($i = 1, 2, \dots, 6$) are the six combined principal invariants of \mathbf{C} and \mathbf{D}_R :

$$\begin{aligned} I_1 &= \text{tr}(\mathbf{C}), \quad I_2 = \text{tr}(\mathbf{C}^2), \quad I_3 = \text{tr}(\mathbf{C}^3), \\ I_4 &= (\mathbf{D}_R \cdot \mathbf{D}_R), \quad I_5 = (\mathbf{D}_R \cdot \mathbf{C} \mathbf{D}_R), \quad I_6 = (\mathbf{D}_R \cdot \mathbf{C}^2 \mathbf{D}_R). \end{aligned} \quad (3.6)$$

Nearly incompressible materials. We begin by denoting the distortional part of \mathbf{F} by

$$\mathbf{F}_{\text{dis}} \stackrel{\text{def}}{=} J^{-1/3} \mathbf{F}, \quad \det \mathbf{F}_{\text{dis}} = 1. \quad (3.7)$$

Correspondingly, let

$$\mathbf{C}_{\text{dis}} \stackrel{\text{def}}{=} (\mathbf{F}_{\text{dis}})^T \mathbf{F}_{\text{dis}} = J^{-2/3} \mathbf{C}, \quad (3.8)$$

denote the distortional (or volume preserving) right Cauchy–Green tensor. Defining the invariants

$$\bar{I}_1 = \text{tr}(\mathbf{C}_{\text{dis}}) \quad \text{and} \quad \bar{I}_2 = \text{tr}(\mathbf{C}_{\text{dis}}^2), \quad (3.9)$$

we consider the free energy to be a function of following revised invariant list:

$$\bar{\mathcal{I}} = (\bar{I}_1, \bar{I}_2, J, I_4, I_5, I_6). \quad (3.10)$$

Further, we assume that the free energy $\hat{\psi}_R(\bar{\mathcal{I}})$ may be written in a separable form as

$$\hat{\psi}_R(\bar{\mathcal{I}}) = \tilde{\psi}_R^{\text{mech}}(\bar{I}_1, \bar{I}_2, J) + \tilde{\psi}_R^{\text{elec}}(I_4, I_5, I_6, J), \quad (3.11)$$

where $\tilde{\psi}_R^{\text{mech}}$ is the change in the free energy due to mechanical deformation and $\tilde{\psi}_R^{\text{elec}}$ is the contribution to the change in the free energy due to electrical polarization.

Mechanical free energy $\tilde{\psi}_R^{\text{mech}}$. In order to model the stress increase due to the stretching and locking of polymer chains at large strains, for the mechanical free energy, we adopt the phenomenological form proposed by Gent (1996),

$$\tilde{\psi}_R^{\text{mech}} = -\frac{1}{2} G I_m \ln \left(1 - \frac{\bar{I}_1 - 3}{I_m} \right) + \frac{1}{2} K (J - 1)^2, \quad (3.12)$$

where G and K are the ground-state shear and bulk moduli, respectively, and I_m represents the upper limit of $(\bar{I}_1 - 3)$ associated with limited chain extensibility of polymeric molecules.

Electrical free energy $\tilde{\psi}_R^{\text{elec}}$. For the electrical free energy, we adopt the form associated with the “ideal dielectric elastomer” (cf. Zhao et al., 2007)

$$\tilde{\psi}_R^{\text{elec}} = \frac{1}{2\epsilon} J^{-1} I_5 = \frac{1}{2\epsilon} J^{-1} \mathbf{D}_R \cdot \mathbf{C} \mathbf{D}_R, \quad (3.13)$$

where ϵ is the constant dielectric permittivity.

Total free energy $\tilde{\psi}_R$, stresses and electric field. Thus the total free energy is given by

$$\tilde{\psi}_R = -\frac{1}{2} G I_m \ln \left(1 - \frac{\bar{I}_1 - 3}{I_m} \right) + \frac{1}{2} K (J - 1)^2 + \frac{1}{2\epsilon} J^{-1} \mathbf{D}_R \cdot \mathbf{C} \mathbf{D}_R. \quad (3.14)$$

Straightforward calculations give the second Piola stress as

$$\mathbf{S} = 2 \frac{\partial \tilde{\psi}_R}{\partial \mathbf{C}} = J^{-2/3} G \left(1 - \frac{\bar{I}_1 - 3}{I_m} \right)^{-1} \left[\mathbf{1} - \frac{1}{3} (\text{tr } \mathbf{C}_{\text{dis}}) \mathbf{C}_{\text{dis}}^{-1} \right] + KJ(J-1) \mathbf{C}^{-1} + \frac{1}{\epsilon} J^{-1} \left[\mathbf{D}_R \otimes \mathbf{D}_R - \frac{1}{2} (\mathbf{D}_R \cdot \mathbf{C} \mathbf{D}_R) \mathbf{C}^{-1} \right]. \quad (3.15)$$

Further, the first Piola stress is given by

$$\mathbf{T}_R = \mathbf{F} \mathbf{S} = J^{-2/3} G \left(1 - \frac{\bar{I}_1 - 3}{I_m} \right)^{-1} \left[\mathbf{F} - \frac{1}{3} (\text{tr } \mathbf{C}) \mathbf{F}^{-\top} \right] + KJ(J-1) \mathbf{F}^{-\top} + \frac{1}{\epsilon} \left[\mathbf{D}_R \otimes \mathbf{D}_R - \frac{1}{2} J (\mathbf{D} \cdot \mathbf{D}) \mathbf{F}^{-\top} \right], \quad (3.16)$$

and the Cauchy stress is given by

$$\mathbf{T} = J^{-1} \mathbf{F} \mathbf{S} \mathbf{F}^\top = J^{-1} G \left(1 - \frac{\bar{I}_1 - 3}{I_m} \right)^{-1} (\mathbf{B}_{\text{dis}})_0 + K(J-1) \mathbf{1} + \frac{1}{\epsilon} \left[\mathbf{D} \otimes \mathbf{D} - \frac{1}{2} (\mathbf{D} \cdot \mathbf{D}) \mathbf{1} \right]. \quad (3.17)$$

Furthermore, the referential electric field is given by

$$\mathbf{E}_R = \frac{\partial \tilde{\psi}_R}{\partial \mathbf{D}_R} = \frac{1}{\epsilon} J^{-1} \mathbf{C} \mathbf{D}_R, \quad (3.18)$$

and the spatial electric field is given by

$$\mathbf{E} = \mathbf{F}^{-\top} \mathbf{E}_R = \frac{1}{\epsilon} \mathbf{D}. \quad (3.19)$$

In practice, it is typically more convenient to work with the stress and electric displacement in terms of the deformation and electric field. Inverting the relations (3.15) through (3.19), we have

$$\begin{aligned} \mathbf{S} &= J^{-2/3} G \left(1 - \frac{\bar{I}_1 - 3}{I_m} \right)^{-1} \left[\mathbf{1} - \frac{1}{3} (\text{tr } \mathbf{C}_{\text{dis}}) \mathbf{C}_{\text{dis}}^{-1} \right] + KJ(J-1) \mathbf{C}^{-1} + \epsilon J \left[\mathbf{C}^{-1} \mathbf{E}_R \otimes \mathbf{E}_R - \frac{1}{2} (\mathbf{E}_R \cdot \mathbf{C}^{-1} \mathbf{E}_R) \mathbf{C}^{-1} \right], \\ \mathbf{T}_R &= J^{-2/3} G \left(1 - \frac{\bar{I}_1 - 3}{I_m} \right)^{-1} \left[\mathbf{F} - \frac{1}{3} (\text{tr } \mathbf{C}) \mathbf{F}^{-\top} \right] + KJ(J-1) \mathbf{F}^{-\top} + \epsilon J \left[\mathbf{E} \otimes \mathbf{C}^{-1} \mathbf{E}_R - \frac{1}{2} (\mathbf{E} \cdot \mathbf{E}) \mathbf{F}^{-\top} \right], \\ \mathbf{T} &= J^{-1} G \left(1 - \frac{\bar{I}_1 - 3}{I_m} \right)^{-1} (\mathbf{B}_{\text{dis}})_0 + K(J-1) \mathbf{1} + \epsilon \left[\mathbf{E} \otimes \mathbf{E} - \frac{1}{2} (\mathbf{E} \cdot \mathbf{E}) \mathbf{1} \right], \end{aligned} \quad (3.20)$$

for the second and first Piola and Cauchy stresses, respectively, and

$$\begin{aligned} \mathbf{D}_R &= \epsilon J \mathbf{C}^{-1} \mathbf{E}_R, \\ \mathbf{D} &= \epsilon \mathbf{E}, \end{aligned} \quad (3.21)$$

for the referential and spatial electric displacements.

4. Numerical solution procedure

In this section, we describe our numerical solution procedure using finite elements in Abaqus/Standard (2010). We begin by summarizing the governing partial differential equations and boundary conditions in both the strong and weak forms.

Governing partial differential equations and boundary conditions. In our simulations, we neglect body forces and volumetric free charge. Under this assumption, the governing partial differential equations consist of the balance of momentum for the first Piola stress,

$$\text{Div } \mathbf{T}_R = \mathbf{0} \quad \text{in } \mathcal{B}_R, \quad (4.1)$$

with \mathbf{T}_R given by (3.20)₂, and Gauss's law for the electric displacement,

$$\text{Div } \mathbf{D}_R = 0 \quad \text{in } \mathcal{B}_R, \quad (4.2)$$

with \mathbf{D}_R given by (3.21)₁. To specify boundary conditions, we introduce the complementary subsurfaces \mathcal{S}_χ and $\mathcal{S}_{\mathbf{t}_R}$ ($\mathcal{S}_\chi \cup \mathcal{S}_{\mathbf{t}_R} = \partial\mathcal{B}_R$, $\mathcal{S}_\chi \cap \mathcal{S}_{\mathbf{t}_R} = \emptyset$), where displacements and surface tractions are prescribed, respectively. Thus, the mechanical boundary conditions on $\partial\mathcal{B}_R$ are given by

$$\chi = \tilde{\chi} \quad \text{on } \mathcal{S}_\chi \quad \text{and} \quad \mathbf{T}_R \mathbf{n}_R = \tilde{\mathbf{t}}_R \quad \text{on } \mathcal{S}_{\mathbf{t}_R}, \quad (4.3)$$

where $\tilde{\chi}$ and $\tilde{\mathbf{t}}_R$ are prescribed. Similarly, we introduce another set of subsurfaces \mathcal{S}_{φ_R} and \mathcal{S}_{ω_R} ($\mathcal{S}_{\varphi_R} \cup \mathcal{S}_{\omega_R} = \partial\mathcal{B}_R$, $\mathcal{S}_{\varphi_R} \cap \mathcal{S}_{\omega_R} = \emptyset$), on which the electric potential and surface charge density are prescribed, respectively. The electrical boundary conditions on $\partial\mathcal{B}_R$ are then given by

$$\varphi = \tilde{\varphi} \quad \text{on } \mathcal{S}_{\varphi_R} \quad \text{and} \quad -\mathbf{D}_R \cdot \mathbf{n}_R = \tilde{\omega} \quad \text{on } \mathcal{S}_{\omega_R}, \quad (4.4)$$

where $\tilde{\varphi}$ and $\tilde{\omega}$ are prescribed.

In writing the boundary conditions (4.3)₂ and (4.4)₂, we have neglected the stress and electric displacement in the region of space surrounding the body \mathcal{B}_R , thereby reducing the boundary conditions with jump conditions, (2.7) and (2.9), to those above. This assumption is made on pragmatic grounds as it greatly simplifies the problem, eliminating the need to account for the surrounding space. However, in the general electromechanical problem, the stress and electric displacement are nonzero in the surroundings. For example, for the well-known case of a surrounding space comprised of a vacuum, the Cauchy stress and electric displacement are given by

$$\mathbf{T} = \epsilon_0 [\mathbf{E} \otimes \mathbf{E} - \frac{1}{2} (\mathbf{E} \cdot \mathbf{E}) \mathbf{1}] \quad \text{and} \quad \mathbf{D} = \epsilon_0 \mathbf{E}, \quad (4.5)$$

respectively, where ϵ_0 is the permittivity of free space. Neglecting this contribution can lead to significant errors for general boundary-value problems. However, in practical applications, most electromechanical transducers made from soft dielectrics consist of a thin layer sandwiched between two flexible electrodes. In this case, the effect of the surroundings is only felt at the edges of the electrodes, which we refer to as fringe effects. In Appendix A, we examine these fringe effects when the surrounding space is taken into account and provide an estimate of the error introduced by neglecting the effect of the surroundings. Our analysis clearly demonstrates that for this commonly used configuration only a very small error is introduced by neglecting the effect of the surroundings.

The coupled set of Eqs. (4.1) and (4.2), together with (4.3) and (4.4), represents the strong form of a boundary-value problem for the motion $\chi(\mathbf{x}_R, t)$ and the electric potential $\varphi(\mathbf{x}_R, t)$. Then with \mathbf{w}_1 and w_2 denoting two weighting (or test) fields, the corresponding weak forms are

$$\begin{aligned} \int_{\mathcal{B}_R} \left(\mathbf{T}_R : \frac{\partial \mathbf{w}_1}{\partial \mathbf{X}} \right) dv_R &= \int_{\mathcal{S}_{\mathbf{t}_R}} (\mathbf{w}_1 \cdot \tilde{\mathbf{t}}_R) da_R, \\ \int_{\mathcal{B}_R} \left(\mathbf{D}_R \cdot \frac{\partial w_2}{\partial \mathbf{X}} \right) dv_R + \int_{\mathcal{S}_{\omega_R}} (w_2 \tilde{\omega}_R) da_R &= 0. \end{aligned} \quad (4.6)$$

Finite-element discretization, element-level residuals and tangents. The body is approximated using finite elements, $\mathcal{B}_R = \cup \mathcal{B}_R^e$. The nodal solution variables are taken to be the displacement and the electric potential, which are interpolated inside each element by

$$\mathbf{u} = \sum \mathbf{u}^A N^A \quad \text{and} \quad \varphi = \sum \varphi^A N^A, \quad (4.7)$$

with the index $A = 1, 2, \dots$ denoting the nodes of the element, \mathbf{u}^A and φ^A nodal displacements and electric potentials, and N^A the shape functions. We employ a standard Galerkin approach, in that the weighting fields are interpolated by the same shape functions,

$$\mathbf{w}_1 = \sum \mathbf{w}_1^A N^A \quad \text{and} \quad w_2 = \sum w_2^A N^A. \quad (4.8)$$

Using (4.7) and (4.8) in (4.6) yields the following element-level system of equations:

$$\begin{aligned} \int_{\mathcal{B}_R^e} \left(\mathbf{T}_R \frac{\partial N^A}{\partial \mathbf{X}} \right) dv_R &= \int_{\mathcal{S}_{\mathbf{t}_R}^e} (N^A \tilde{\mathbf{t}}_R) da_R, \\ \int_{\mathcal{B}_R^e} \left(\mathbf{D}_R \cdot \frac{\partial N^A}{\partial \mathbf{X}} \right) dv_R + \int_{\mathcal{S}_{\omega_R}^e} (N^A \tilde{\omega}_R) da_R &= 0. \end{aligned} \quad (4.9)$$

This system of coupled equations is solved iteratively using a Newton procedure by defining the following element-level residuals for the displacement and electric potential:

$$\begin{aligned} (\mathbf{R}_u)^A &= - \int_{\mathcal{B}_R^e} \left(\mathbf{T}_R \frac{\partial N^A}{\partial \mathbf{X}} \right) dv_R + \int_{\mathcal{S}_{\mathbf{t}_R}^e} (N^A \tilde{\mathbf{t}}_R) da_R, \\ (R_\varphi)^A &= \int_{\mathcal{B}_R^e} \left(\mathbf{D}_R \cdot \frac{\partial N^A}{\partial \mathbf{X}} \right) dv_R + \int_{\mathcal{S}_{\omega_R}^e} (N^A \tilde{\omega}_R) da_R, \end{aligned} \quad (4.10)$$

and using the corresponding tangents

$$\begin{aligned} (\mathbf{K}_{\mathbf{u}\mathbf{u}})^{AB} &= -\frac{\partial(\mathbf{R}_{\mathbf{u}})^A}{\partial \mathbf{u}^B}, & (\mathbf{K}_{\mathbf{u}\varphi})^{AB} &= -\frac{\partial(\mathbf{R}_{\mathbf{u}})^A}{\partial \varphi^B}, \\ (\mathbf{K}_{\varphi\mathbf{u}})^{AB} &= -\frac{\partial(R_\varphi)^A}{\partial \mathbf{u}^B}, & (K_{\varphi\varphi})^{AB} &= -\frac{\partial(R_\varphi)^A}{\partial \varphi^B}. \end{aligned} \quad (4.11)$$

Switching to index notation for ease of presentation, we have

$$\begin{aligned} K_{u_i u_k}^{AB} &= -\frac{\partial R_{u_i}^A}{\partial u_k^B}, & K_{u_i \varphi}^{AB} &= -\frac{\partial R_{u_i}^A}{\partial \varphi^B}, \\ K_{\varphi u_k}^{AB} &= -\frac{\partial R_\varphi^A}{\partial u_k^B}, & K_{\varphi \varphi}^{AB} &= -\frac{\partial R_\varphi^A}{\partial \varphi^B}. \end{aligned} \quad (4.12)$$

Evaluating for a case in which the surface traction and surface charge density are fixed, we have

$$\begin{aligned} K_{u_i u_k}^{AB} &= \int_{\mathcal{B}_t^e} \frac{\partial N^A}{\partial X_j} \frac{\partial T_{R,ij}}{\partial F_{kl}} \frac{\partial N^B}{\partial X_l} dv_R, \\ K_{u_i \varphi}^{AB} &= \int_{\mathcal{B}_t^e} \frac{\partial N^A}{\partial X_j} \frac{\partial T_{R,ij}}{\partial E_{R,l}} \frac{\partial N^B}{\partial X_l} dv_R, \\ K_{\varphi u_k}^{AB} &= - \int_{\mathcal{B}_t^e} \frac{\partial N^A}{\partial X_j} \frac{\partial D_{R,j}}{\partial F_{kl}} \frac{\partial N^B}{\partial X_l} dv_R, \\ K_{\varphi \varphi}^{AB} &= - \int_{\mathcal{B}_t^e} \frac{\partial N^A}{\partial X_j} \frac{\partial D_{R,j}}{\partial E_{R,l}} \frac{\partial N^B}{\partial X_l} dv_R. \end{aligned} \quad (4.13)$$

For completeness, we include the non-standard material tangents below:

$$\begin{aligned} \frac{\partial T_{R,ij}^{\text{elec}}}{\partial F_{kl}} &= J\epsilon \left(-F_{li}^{-1} C_{jm}^{-1} E_{R,m} E_k - E_i F_{jk}^{-1} C_{lm}^{-1} E_{R,m} - E_i E_k C_{jl}^{-1} + F_{ji}^{-1} E_k C_{lm}^{-1} E_{R,m} \right. \\ &\quad \left. + E_i C_{jm}^{-1} E_{R,m} F_{lk}^{-1} + \frac{1}{2} E_m E_m F_{li}^{-1} F_{jk}^{-1} - \frac{1}{2} E_m E_m F_{ji}^{-1} F_{lk}^{-1} \right), \\ \frac{\partial T_{R,ij}}{\partial E_{R,l}} &= J\epsilon (F_{li}^{-1} C_{jm}^{-1} E_{R,m} + E_i C_{jl}^{-1} - F_{ji}^{-1} C_{lm}^{-1} E_{R,m}), \\ \frac{\partial D_{R,j}}{\partial F_{kl}} &= -J\epsilon (F_{jk}^{-1} C_{lm}^{-1} E_{R,m} + E_k C_{jl}^{-1} - C_{jm}^{-1} E_{R,m} F_{lk}^{-1}), \\ \frac{\partial D_{R,j}}{\partial E_{R,l}} &= J\epsilon C_{jl}^{-1}, \end{aligned} \quad (4.14)$$

where $\mathbf{T}_R^{\text{elec}} = 2\mathbf{F}(\partial \tilde{\nu}_R^{\text{elec}} / \partial \mathbf{C})$.

Finite-element formulation in the spatial configuration. Here we summarize the corresponding finite-element numerical procedure formulated in the spatial configuration rather than in the reference configuration as in the previous section. In the absence of body forces and volumetric free charge density, the governing partial differential equations, expressed in the deformed body \mathcal{B}_t , consist of the balance of momentum,

$$\text{div} \mathbf{T} = \mathbf{0} \quad \text{in } \mathcal{B}_t, \quad (4.15)$$

with \mathbf{T} given by (3.20)₃, and Gauss's law,

$$\text{div} \mathbf{D} = 0 \quad \text{in } \mathcal{B}_t, \quad (4.16)$$

with \mathbf{D} given by (3.21)₂. The mechanical boundary conditions on $\partial \mathcal{B}_t$ are given by

$$\mathbf{u} = \tilde{\mathbf{u}} \quad \text{on } \mathcal{S}_{\mathbf{u}} \quad \text{and} \quad \mathbf{T}\mathbf{n} = \tilde{\mathbf{t}} \quad \text{on } \mathcal{S}_{\mathbf{t}}, \quad (4.17)$$

where $\tilde{\mathbf{u}}$ and $\tilde{\mathbf{t}}$ are the prescribed displacements and spatial surface tractions, respectively, $\mathcal{S}_{\mathbf{u}}$ and $\mathcal{S}_{\mathbf{t}}$ are complementary subsurfaces of $\partial \mathcal{B}_t$ and \mathbf{n} is the outward unit normal on $\partial \mathcal{B}_t$. The electrical boundary conditions on $\partial \mathcal{B}_t$ are then given by

$$\varphi = \tilde{\varphi} \quad \text{on } \mathcal{S}_\varphi \quad \text{and} \quad -\mathbf{D} \cdot \mathbf{n} = \tilde{\omega} \quad \text{on } \mathcal{S}_\omega, \quad (4.18)$$

where $\tilde{\varphi}$ and $\tilde{\omega}$ are the prescribed electric potentials and spatial surface charge density, respectively, and \mathcal{S}_φ and \mathcal{S}_ω are another set of complementary subsurfaces of $\partial \mathcal{B}_t$. The coupled set of equations (4.15) and (4.16), along with the boundary conditions (4.17) and (4.18), represents the strong form of the spatial boundary-value problem for the displacements and the

electric potential. Then with \mathbf{w}_1 and w_2 denoting two weighting fields, the corresponding weak forms are

$$\begin{aligned} \int_{B_t} \left(\mathbf{T} : \frac{\partial \mathbf{w}_1}{\partial \mathbf{x}} \right) dv &= \int_{S_t} (\mathbf{w}_1 \cdot \dot{\mathbf{t}}) da, \\ \int_{B_t} \left(\mathbf{D} \cdot \frac{\partial w_2}{\partial \mathbf{x}} \right) dv + \int_{S_o} (w_2 \dot{\omega}) da &= 0. \end{aligned} \quad (4.19)$$

Using the standard Galerkin approach with shape functions N^A as in the previous section, we arrive at the following element-level residuals for the displacement and electric potential:

$$\begin{aligned} (\mathbf{R}_u)^A &= - \int_{B_t^e} \left(\mathbf{T} \cdot \frac{\partial N^A}{\partial \mathbf{x}} \right) dv + \int_{S_t^e} (N^A \dot{\mathbf{t}}) da, \\ (R_\phi)^A &= \int_{B_t^e} \left(\mathbf{D} \cdot \frac{\partial N^A}{\partial \mathbf{x}} \right) dv + \int_{S_o^e} (N^A \dot{\omega}) da. \end{aligned} \quad (4.20)$$

Evaluating the corresponding tangents in the absence of surface tractions and surface charge density, we have

$$\begin{aligned} K_{u_i u_k}^{AB} &= \int_{B_t^e} \frac{\partial N^A}{\partial x_j} \left(J^{-1} F_{jm} F_{ln} \frac{\partial T_{R,im}}{\partial F_{kn}} \right) \frac{\partial N^B}{\partial x_l} dv, \\ K_{u_i \phi}^{AB} &= \int_{B_t^e} \frac{\partial N^A}{\partial x_j} \left(J^{-1} F_{jm} F_{ln} \frac{\partial T_{R,im}}{\partial E_{R,n}} \right) \frac{\partial N^B}{\partial x_l} dv, \\ K_{\phi u_k}^{AB} &= - \int_{B_t^e} \frac{\partial N^A}{\partial x_j} \left(J^{-1} F_{jm} F_{ln} \frac{\partial D_{R,m}}{\partial F_{kn}} \right) \frac{\partial N^B}{\partial x_l} dv, \\ K_{\phi \phi}^{AB} &= - \int_{B_t^e} \frac{\partial N^A}{\partial x_j} \left(J^{-1} F_{jm} F_{ln} \frac{\partial D_{R,m}}{\partial E_{R,n}} \right) \frac{\partial N^B}{\partial x_l} dv. \end{aligned} \quad (4.21)$$

Finally, the non-standard spatial tangents are

$$\begin{aligned} J^{-1} F_{jm} F_{ln} \frac{\partial T_{R,im}^{\text{elect}}}{\partial F_{kn}} &= \epsilon \left(-\delta_{il} E_j E_k - E_i \delta_{jk} E_l - E_i E_k \delta_{jl} + \delta_{ij} E_k E_l + E_i E_j \delta_{kl} + \frac{1}{2} E_m E_m \delta_{il} \delta_{jk} - \frac{1}{2} E_m E_m \delta_{ij} \delta_{kl} \right), \\ J^{-1} F_{jm} F_{ln} \frac{\partial T_{R,im}}{\partial E_{R,n}} &= \epsilon (\delta_{il} E_j + E_i \delta_{jl} - \delta_{ij} E_l), \\ J^{-1} F_{jm} F_{ln} \frac{\partial D_{R,m}}{\partial F_{kn}} &= -\epsilon (\delta_{jk} E_l + E_k \delta_{jl} - E_j \delta_{kl}), \\ J^{-1} F_{jm} F_{ln} \frac{\partial D_{R,m}}{\partial E_{R,n}} &= \epsilon \delta_{jl}. \end{aligned} \quad (4.22)$$

The finite-element procedures have been implemented in [Abaqus/Standard \(2010\)](#) using a user-element subroutine (UEL) and employing the spatial finite-element formulation. During an analysis, the user subroutine UEL is called for each iteration in a given increment. The initial nodal coordinates as well as the current guesses of the nodal displacements and electric potentials are passed into the subroutine, and the nodal residuals (4.20) and consistent tangents (4.21) are required as outputs. We have developed four-noded isoparametric quadrilateral plane-strain and axisymmetric user-elements, as well as an eight-noded continuum brick user-element. In order to avoid issues related to volumetric-locking, we utilize the F-bar method of [de Souza Neto et al. \(1996\)](#) for fully integrated elements.² We have made our Abaqus user-element subroutines available online as supplementary material.

5. Numerical simulations

In this section, we demonstrate our numerical simulation capability in a variety of settings (three-dimensional, plane-strain and axisymmetric) and in several interesting applications. We begin by verifying the numerical implementation of each of our elements by comparing analytical expressions against single-element simulations. Then, we consider the following list of applications:

- a torsional actuator,
- a bending actuator,
- a barrel-type energy harvesting device and
- a diaphragm-type energy harvesting device.

² For a similar usage of the Abaqus UEL capability, see [Chester and Anand \(2011\)](#).

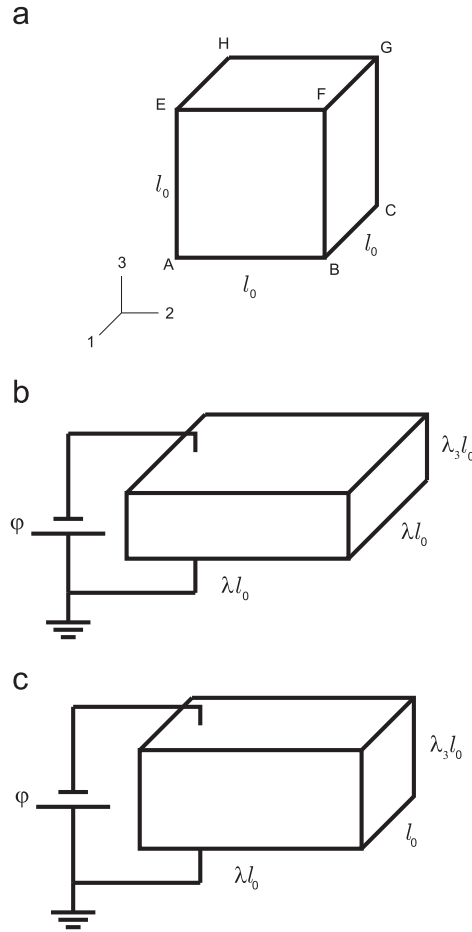


Fig. 1. (a) An undeformed cube with side length l_0 . (b) Homogeneous, one-dimensional actuation with $\lambda_1 = \lambda_2 = \lambda$. For the incompressible case, $\lambda_3 = 1/\lambda^2$. (c) Homogeneous, one-dimensional, plane-strain actuation with $\lambda_1 = 1$ and $\lambda_2 = \lambda$. For the incompressible case, $\lambda_3 = 1/\lambda$.

5.1. Single-element verification

First, in order to verify our finite-element implementation, we demonstrate that single-element simulations of homogeneous, one-dimensional actuation replicate analytical results.

The first case we consider is that of *axisymmetric*, one-dimensional actuation. This will allow us to verify our eight-noded brick element as well as our four-noded axisymmetric element. Consider a block in the shape of a cube with side length l_0 as pictured in Fig. 1(a).³ The mechanical deformation is constrained so that the principal stretches are aligned along each edge of the cube and so that $\lambda_1 = \lambda_2 = \lambda$, as pictured in Fig. 1(b). The electric potential is held at zero on face ABCD, and an electric potential of φ is applied to face EFGH. All faces are traction-free, so that all components of the stress are zero.

This case was simulated both with a single eight-noded brick element and a single four-noded axisymmetric element. We nondimensionalize our simulation results by the shear modulus G and the permittivity ϵ , and to model nearly incompressible behavior, we take $K/G = 1000$. It is well known that, under these loading conditions, a snap-through-type, electromechanical instability typically occurs along the direction of the applied electric field (in this case, the three direction). It may be shown that this instability is suppressed in a Gent material for $I_m \lesssim 7.308$. As such, we consider $I_m = 1, 2, 3, 4, 5, 6$ and 7 . For comparison, we consider the analytical solution for this case of one-dimensional actuation under ideally incompressible conditions, derived in Section B.1 (cf. (B.4)),

$$\frac{\varphi}{l_0} \sqrt{\frac{\epsilon}{G}} = \sqrt{\left(1 - \frac{2\lambda^2 + (1/\lambda^4) - 3}{I_m}\right)^{-1} \frac{1}{\lambda^2} \left(1 - \frac{1}{\lambda^6}\right)}, \quad (5.1)$$

³ A soft dielectric actuator in the shape of a cube would be subject to significant fringe effects, cf. Appendix A, and require an accounting of the surroundings to accurately model its actuation. However, the intent of our single-element verification is to compare simulation results to homogeneous, analytical solutions, and as such, we neglect the surroundings. One may think of the block of material as being extracted from a much larger specimen far from any boundaries so that the deformation and electric field are homogeneous.

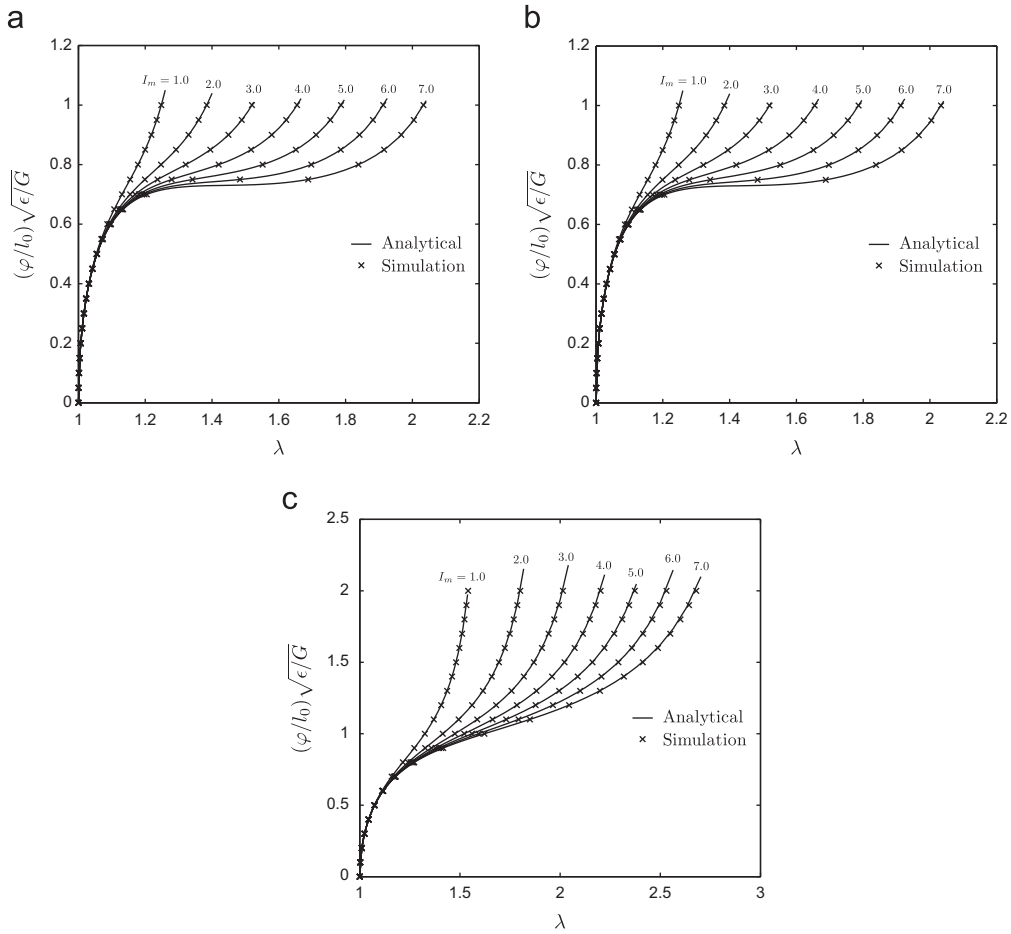


Fig. 2. Normalized electric potential versus lateral stretch for (a) three-dimensional, (b) axisymmetric, and (c) plane-strain elements and different values of I_m .

where λ is the lateral stretch, defined in the preceding paragraph. In Fig. 2(a) and (b), we plot the simulated actuation response (lateral stretch λ versus normalized electric field $(\varphi/l_0)\sqrt{\epsilon/G}$ versus (5.1) for the eight-noded brick element and the four-noded axisymmetric element, respectively, verifying that these elements accurately reproduce the response of a Gent material.

Finally, we consider *plane-strain*, one-dimensional actuation in order to verify our four-noded plane-strain element. Beginning with the same cube of material in Fig. 1(a), we consider the plane-strain deformation shown in Fig. 1(c). The mechanical and electrical boundary conditions are applied in the same manner as the previous case but with the constraint $\lambda_1 = 1$. As before, we denote the lateral stretch $\lambda_2 = \lambda$. No electromechanical instability occurs in plane-strain, but for the sake of consistency, we again take $I_m = 1, 2, 3, 4, 5, 6$ and 7 . The analytical solution for plane-strain, one-dimensional actuation under ideally incompressible conditions is derived in Section B.2 (cf. (B.8)),

$$\frac{\varphi}{l_0}\sqrt{\frac{\epsilon}{G}} = \sqrt{\left(1 - \frac{\lambda^2 + (1/\lambda^2) - 2}{I_m}\right)^{-1} \left(1 - \frac{1}{\lambda^4}\right)}. \quad (5.2)$$

In Fig. 2(c), we plot the simulated actuation response for the four-noded plane-strain element against (5.2), verifying the element.

With verified elements in hand, we turn to consider several applications. Throughout, we continue to take $K/G = 1000$ to model nearly incompressible behavior, and we leave G and ϵ unspecified and normalize our simulation results by these parameters. It is not our interest here to consider the electromechanical, snap-through instability, and as such, we take $I_m = 7$. We acknowledge that this value is rather low compared to real dielectric elastomeric materials.

5.2. Torsional actuator

As a demonstration of our simulation capability in a three-dimensional setting that cannot be analytically addressed, we consider an actuator designed to produce twisting motion. To this end, we consider a thin strip of dielectric elastomer of

thickness t_0 and width w_0 in a helicoid shape consisting of one full twist over a length of L_0 .⁴ Fig. 3(a) shows the undeformed finite-element configuration, consisting of 4720 eight-noded continuum brick elements with two elements through the thickness, for $L_0/w_0 = 5$ and $w_0/t_0 = 10$. We also considered cases of $L_0/w_0 = 3, 4$ and 6 and $w_0/t_0 = 10$, consisting of 3440, 4040 and 5400 elements, respectively.

For mechanical boundary conditions, the face EFGH is constrained to remain planar and not rotate; however, the face is allowed to change width and thickness. Likewise, the face ABCD is constrained to remain planar and allowed to change width and thickness, but it is also allowed to rotate about the three-axis. The electric potential degrees of freedom on the face CDHG are held at zero, while an electric potential of φ is applied to face ABFE, as shown in Fig. 3(b). The final maximum value of the dimensionless normalized electric potential $(\varphi/t_0)\sqrt{\epsilon/G}$ is 0.5.

The deformed configuration for $L_0/w_0 = 5$ is shown in Fig. 3(b). In response to the applied electric potential, the helicoid strip reduces in thickness, while increasing in length and width. As a result the front face rotates by an angle denoted by θ . Fig. 3(c) shows the actuation response θ in radians as a function of the normalized electric potential $(\varphi/t_0)\sqrt{\epsilon/G}$ for the four values of L_0/w_0 , demonstrating a nonlinear, monotonic response. The nonlinear nature of the actuation response in all cases is due to the quadratic dependence of the stress on the electric field, cf. (3.20). Further, we note that for smaller values of L_0/w_0 , i.e. more tightly wound helicoids, more twist is attained at the same applied electric potential. Thus, we have used our three-dimensional simulation capability to address a torsional actuator.

5.3. Bending actuator

Next, we consider a plane-strain actuator capable of producing bending motion in response to an applied electric potential. Specifically, we consider a bilayer, consisting of two layers of thickness t_0 and length L_0 , as shown in Fig. 4(a). With reference to this figure, layer FCDE is dielectric elastomer, and layer ABCF is an elastomeric substrate, which we take to be a Gent material with shear modulus G_{sub} and $I_m = 7$. The finite-element mesh, shown in Fig. 4(a), consists of 1000 four-noded quadrilateral plane-strain elements. We set $L_0/t_0 = 20$ and take $G_{\text{sub}}/G = 1$.

On side AFE, we set the horizontal displacement to be zero, $u_1 = 0$, and pin the node F. The nodes along the side BCD are constrained to remain linear but may reduce in thickness so that the resulting deformation is pure bending. The electric potential along side FC is held at zero, while an electric potential of φ is applied to side ED, as shown in Fig. 4(b). The final maximum value of the normalized electric potential $(\varphi/t_0)\sqrt{\epsilon/G}$ is again 0.5.

The deformed configuration is shown in Fig. 4(b). The applied electric potential causes the top layer to reduce thickness and expand length, while the bottom layer resists the increase in length. The result is that the bilayer takes on a curvature κ , or equivalently goes through an angle of bending $L_0\kappa$. Fig. 4(c) shows the bending angle $L_0\kappa$ in radians as a function of the normalized electric potential, and again a nonlinear, monotonic response is observed.

Finally, we examine the effect of the ratio of the shear modulus of the substrate G_{sub} to that of the dielectric elastomer G . Fig. 4(d) shows the bending angle $L_0\kappa$ as a function of the ratio G_{sub}/G for several values of the normalized electric potential, $(\varphi/t_0)\sqrt{\epsilon/G} = 0.3, 0.4$ and 0.5 . It is evident that the actuation response is maximized for $G_{\text{sub}}/G \approx 1$. When the substrate is significantly stiffer than the dielectric elastomer, $G_{\text{sub}}/G \gg 1$, the actuation of the dielectric elastomer cannot significantly move the substrate. For the case of a compliant substrate, $G_{\text{sub}}/G \ll 1$, the actuation of the dielectric elastomer causes the substrate to reduce thickness and increase length rather than bend. Thus, when G_{sub} and G are approximately equal maximal actuation may be attained. This exercise demonstrates the use of our plane-strain simulation capability to design a bending actuator.

5.4. Barrel-type energy harvesting device

To this point, we have considered actuators, i.e. devices that convert electrical work into mechanical motion. Next, we turn our attention to energy harvesting devices. Energy harvesting devices are designed to convert mechanical work into electrical energy, while undergoing a repeated cycle. Here, we consider an energy harvesting device in a barrel shape. Energy harvesting devices of this type have been used to harvest energy from wave motion to power buoys (Kornbluh et al., 2011). We consider a barrel shape with inner radius R_0 , thickness t_0 and length L_0 and take $R_0/t_0 = 20$ and $L_0/t_0 = 40$. Employing an axisymmetric simplification, the initial finite-element mesh is shown in Fig. 5(a), consisting of 1000 four-noded quadrilateral axisymmetric elements with five elements through the thickness.

Throughout the cycle, the nodes along side AB are constrained to $u_2 = 0$ and node A is pinned. The nodes along side CD are constrained to have the same displacement in the two-direction, while $u_1 = 0$ is set for node D. The mechanical part of the cycle is conducted in force-control with a force F applied in the two-direction on the side CD. The side AD is set to ground with an electric potential of zero, and side BC is constrained such that all nodes along that side have the same electric potential. The electrical part of the cycle is conducted in charge-control with a total charge $-Q$ applied to the side BC. The control parameters F and Q are then prescribed to complete a cycle. The dependent variables throughout the cycle are the displacement of the face CD in the two-direction δ and the electric potential on face BC φ .

The cycle is prescribed as follows:

⁴ For a similar type of actuator, see Carpi et al. (2005).

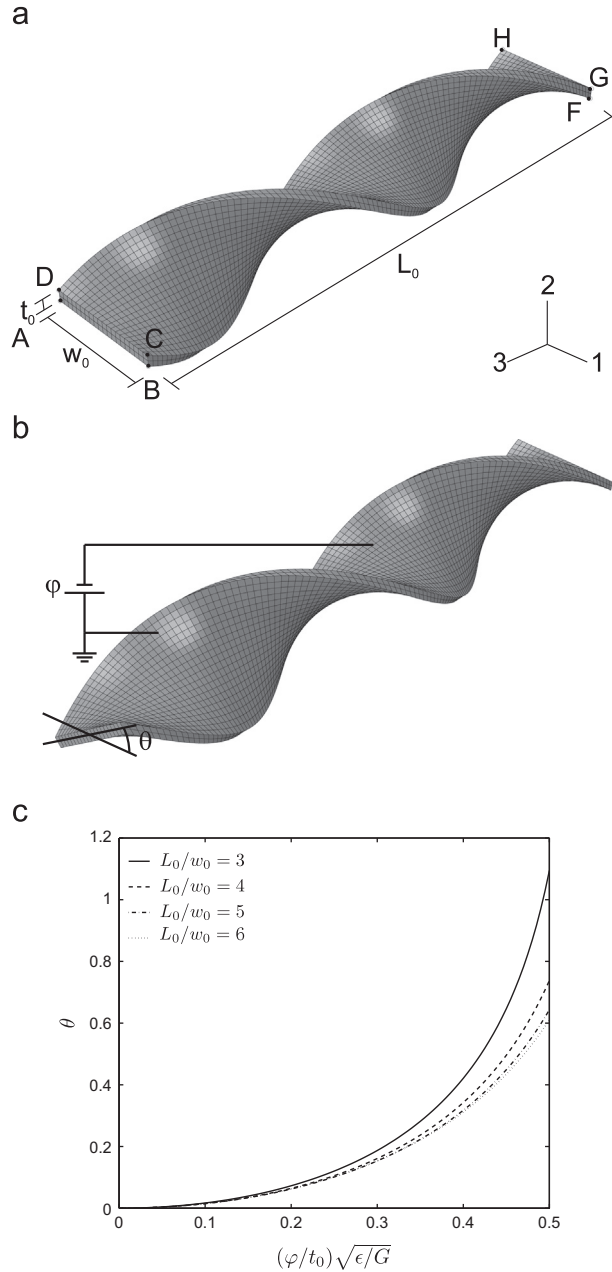


Fig. 3. Schematic of the (a) undeformed and (b) deformed configurations for a twisting actuator with $L_0/w_0 = 5$. (c) Twist angle in radians versus normalized electric potential for four different values of L_0/w_0 .

- State 1: A prestretch is imparted by applying a force F_{low} to the face CD, and no charge is applied to face BC so that the electric potential difference through thickness is zero, cf. Fig. 5(b).
- State 2: The force is ramped to its maximum value F_{high} while the circuit remains open so that the charge stays fixed at zero, cf. Fig. 5(c).
- State 3: The force is fixed at F_{high} while a charge of Q_{high} is applied. As a result the barrel reduces in thickness, and the displacement of the face CD δ increases, cf. Fig. 5(d).
- State 4: The force is reduced to F_{low} while the circuit is left open so that the charge Q_{high} remains fixed. Reducing the force causes δ to decrease and the thickness of the barrel to increase, thereby moving the charge farther apart. Moving the charge apart increases the electric potential difference across the thickness φ , cf. Fig. 5(e).
- State 1: To complete the cycle, the charge is removed so that the electric potential difference through thickness returns to zero, while the force is fixed at F_{low} , cf. Fig. 5(b).

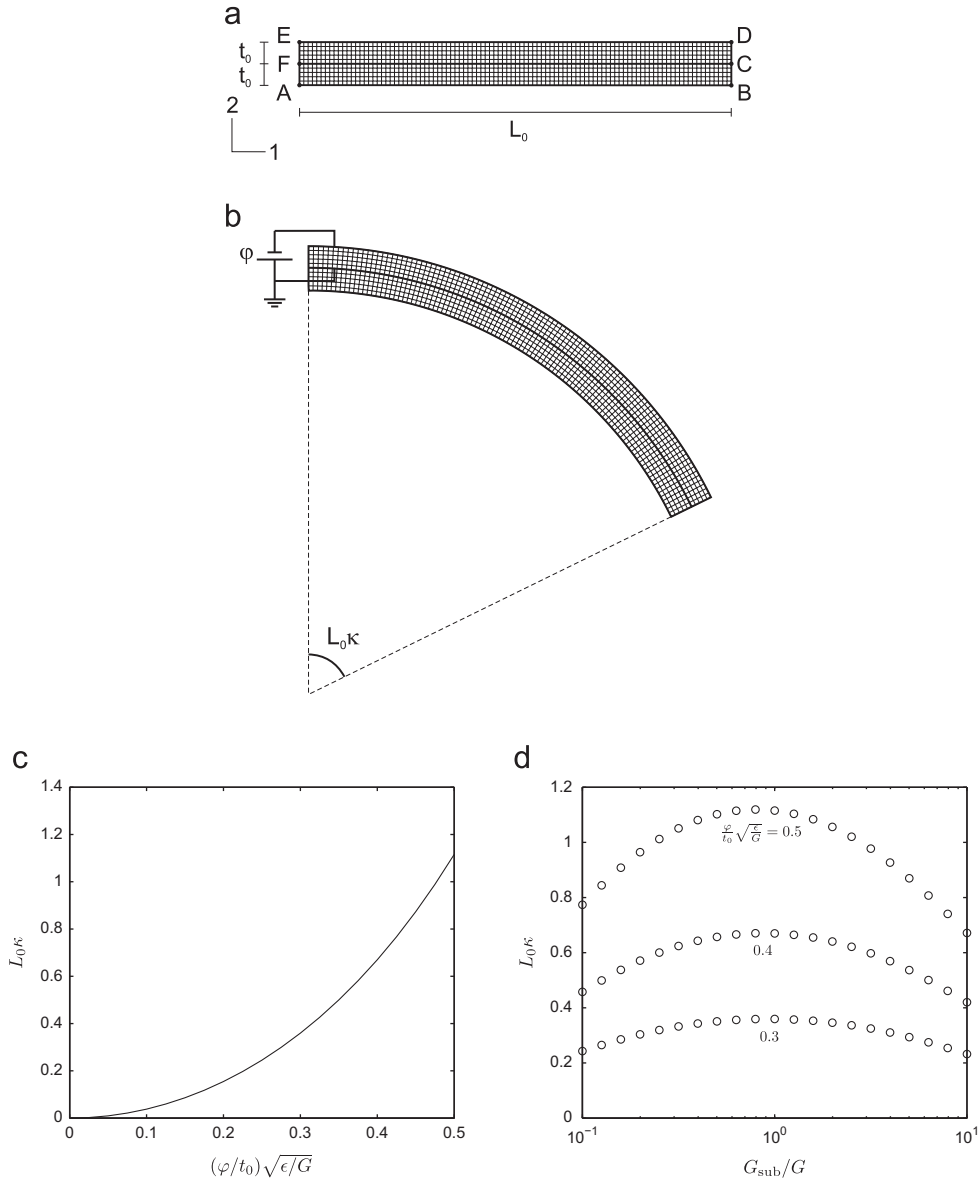


Fig. 4. Schematic of the (a) undeformed and (b) deformed configurations for a plane-strain bending actuator. (c) Bend angle in radians versus normalized electric potential for $G_{sub}/G = 1$. (d) Bend angle versus the shear modulus ratio G_{sub}/G for three values of the normalized electric potential.

In summary, the steps 1–2 and 3–4 represent mechanical loading without charge and unloading under charge, respectively. Steps 2–3 and 4–1 represent charging and uncharging under fixed load, respectively.

To analyze this cycle, we employ two sets of dimensionless work conjugate variables: a mechanical set, consisting of a normalized force $F/(2\pi R_0 t_0 G)$ and a normalized displacement δ/L_0 , and an electrical set, consisting of a normalized electric potential $(\varphi/t_0)\sqrt{\epsilon/G}$ and a normalized charge $Q/(2\pi R_0 L_0 \sqrt{G\epsilon})$. We take $F_{high}/(2\pi R_0 t_0 G) = 2.05$, $F_{low}/F_{high} = 0.5$, and $Q_{high}/(2\pi R_0 L_0 \sqrt{G\epsilon}) = 0.8492$. The mechanical and electrical variables are plotted against each other in Fig. 5(f) and (g), respectively. The four states are labeled on each diagram. The force-displacement cycle is traversed in a clockwise manner, indicating that mechanical work is expended over the cycle. Conversely, the electric potential-charge diagram is traversed counterclockwise, indicating that electrical energy is harvested. Of importance is the step 3–4, which involves mechanical unloading at fixed charge. It is this step that raises the electric potential and allows electrical energy to be harvested. We may determine the amount of energy transformed from mechanical work to electrical energy per cycle, denoted by W , by considering the area enclosed by each loop. Since we have considered an “ideal” dielectric elastomer, which exhibits no dissipation through viscoelastic behavior or dielectric relaxation, all of the mechanical work is transformed into electrical energy (i.e. the system has an efficiency of unity) and hence the areas enclosed by both loops are equal. From Fig. 5(f) and (g), we determine the amount of energy transformed to be $W = 0.0618(2\pi R_0 L_0 t_0 G)$.

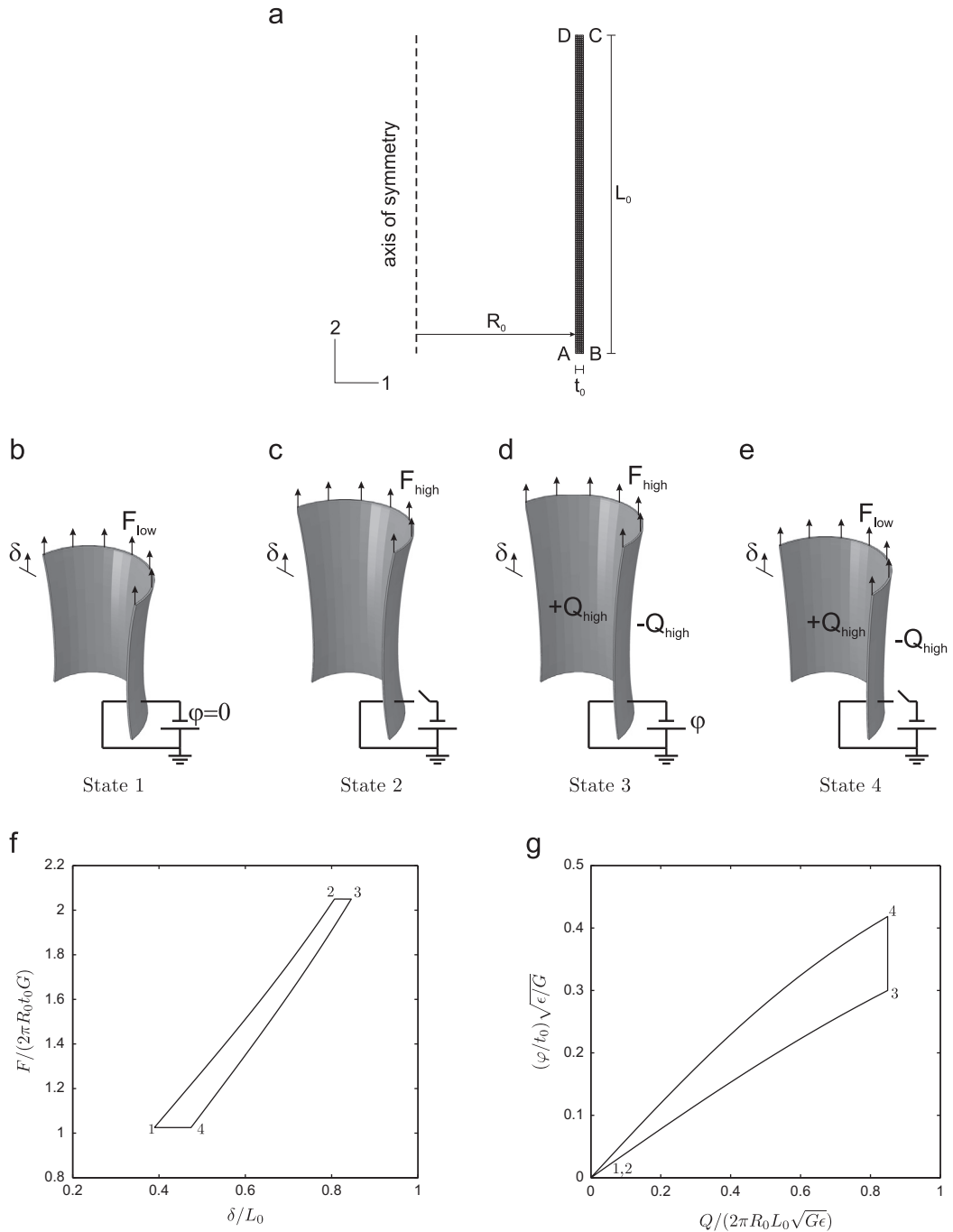


Fig. 5. (a) Initial axisymmetric finite-element mesh for a barrel-type energy harvesting device. (b)–(e) The deformed configuration for the four states of the energy harvesting cycle. Half of the barrel is visualized for clarity. (f) Force-displacement and (g) electric potential-charge diagrams for the cycle with the four states labeled.

The effect of process loading parameters F_{low} , F_{high} , and Q_{high} on the transformed energy per cycle W may be examined with our simulation capability. Fig. 6 summarizes the results of a parametric study. The normalized energy transformed per cycle $W/(2\pi R_0 L_0 t_0 G)$ is plotted as a function of the maximum force $F_{high}/(2\pi R_0 t_0 G)$ for maximum charge $Q_{high}/(2\pi R_0 L_0 \sqrt{\epsilon G}) = 0.6, 0.8, 1.0$ and force ratios (a) $F_{low}/F_{high} = 0.25$ and (b) $F_{low}/F_{high} = 0.5$. Each marker represents the result of an individual simulation and the lines are introduced to guide the eye. We observe that higher amounts of energy are transformed for higher maximum charge and lower force ratios. (Note the different vertical axis scale bars in Fig. 6(a) and (b)). We also observe that the transformed energy first increases then decreases with increasing maximum force, regardless of the maximum charge or force ratio. The decrease in energy transformed for higher values of F_{high} is due to the onset of

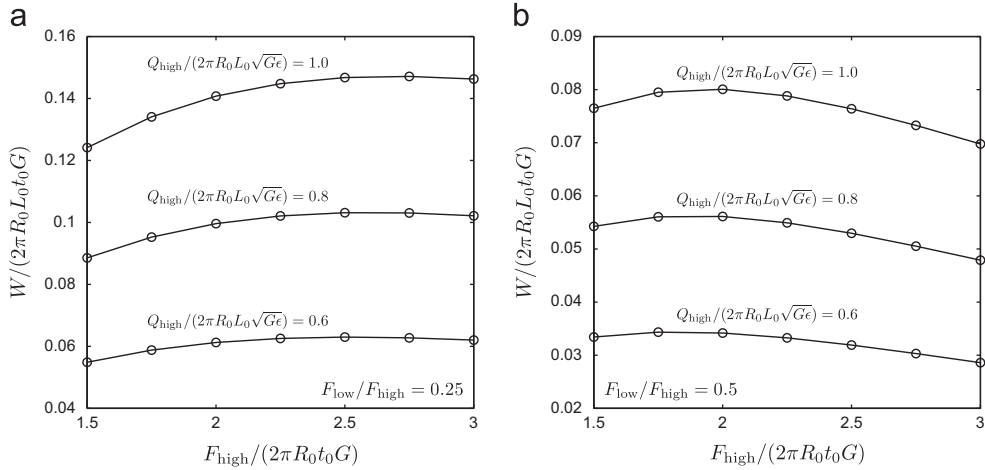


Fig. 6. Normalized energy transformed $W/(2\pi R_0 L_0 t_0 G)$ as function of the maximum force $F_{\text{high}}/(2\pi R_0 t_0 G)$ and maximum charge $Q_{\text{high}}/(2\pi R_0 L_0 \sqrt{G\epsilon})$ for force ratios (a) $F_{\text{low}}/F_{\text{high}} = 0.25$ and (b) $F_{\text{low}}/F_{\text{high}} = 0.5$ for the barrel-type energy harvesting device.

limited chain extensibility effects (or chain-locking), governed by the material parameter I_m in the Gent model used here. That is to say, prior to chain-locking, increasing F_{high} leads to an increase in W , but increasing F_{high} during chain-locking causes a decrease in W . The value of F_{high} corresponding to maximum transformed energy will therefore depend upon I_m in addition to the observed dependence on force ratio and relative insensitivity to Q_{high} . Thus, this example clearly shows that our simulation capability may be used to effectively guide the design and optimization of these devices. As a final comment, we note that, by including material dissipation arising due to viscoelasticity and dielectric relaxation, the efficiency of energy transformation may be investigated.

5.5. Diaphragm-type energy harvesting device

Finally, we consider a second energy harvesting device in the shape of a thin disk with radius R_0 and thickness t_0 that acts as a diaphragm, against which a pressure may be imposed. Energy harvesting devices of this type have been placed in the heels of boots to harvest energy from walking motion to power portable electronic devices (Kornbluh et al., 2011). We take $R_0/t_0 = 20$ and again make an axisymmetric simplification. The initial finite-element mesh is shown in Fig. 7(a), consisting of 500 four-noded quadrilateral axisymmetric elements with five elements through the thickness.

The nodes along side AB are set to have $u_1 = 0$, and the nodes along side CD are set to $u_1 = u_2 = 0$. The mechanical part of the cycle is conducted in pressure control with a live pressure load P applied to side AC. The side AC is also set to ground with an electric potential of zero, and side BD is constrained such that all nodes along that side have the same electric potential. The electrical part of the cycle is again conducted in charge-control with a total charge $-Q$ applied to the side BD. The control parameters P and Q are then prescribed to complete a cycle. The dependent variables throughout the cycle are the volume displaced by the motion of the diaphragm V and the electric potential on face BD φ .

The cycle is prescribed as follows:

- State 1: A prestretch is imparted by applying a pressure P_{low} to the face AC, and no charge is applied to face BD so that the electric potential difference through thickness is zero, cf. Fig. 7(b).
- State 2: The pressure is ramped to its maximum value P_{high} while the circuit remains open so that the charge stays fixed at zero, cf. Fig. 7(c).
- State 3: The pressure is fixed at P_{high} while a charge of Q_{high} is applied. As a result the diaphragm reduces in thickness, and the volume displaced by the diaphragm V increases, cf. Fig. 7(d).
- State 4: The pressure is reduced to P_{low} while the circuit is left open so that the charge Q_{high} remains fixed. Reducing the pressure causes V to decrease and the thickness of the diaphragm to increase, thereby moving the charge farther apart. Moving the charge apart increases the electric potential difference across the thickness φ , cf. Fig. 7(e).
- State 1: To complete the cycle, the charge is removed so that the electric potential difference through thickness returns to zero, while the pressure is fixed at P_{low} , cf. Fig. 7(b).

In summary, the steps 1–2 and 3–4 represent mechanical loading without charge and unloading under charge, respectively. Steps 2–3 and 4–1 represent charging and uncharging under fixed load, respectively.

To analyze this cycle, we employ two sets of dimensionless work conjugate variables: a mechanical set, consisting of a normalized pressure P/G and a normalized volume $V/(\pi R_0^2 t_0)$, and an electrical set, consisting of a normalized electric

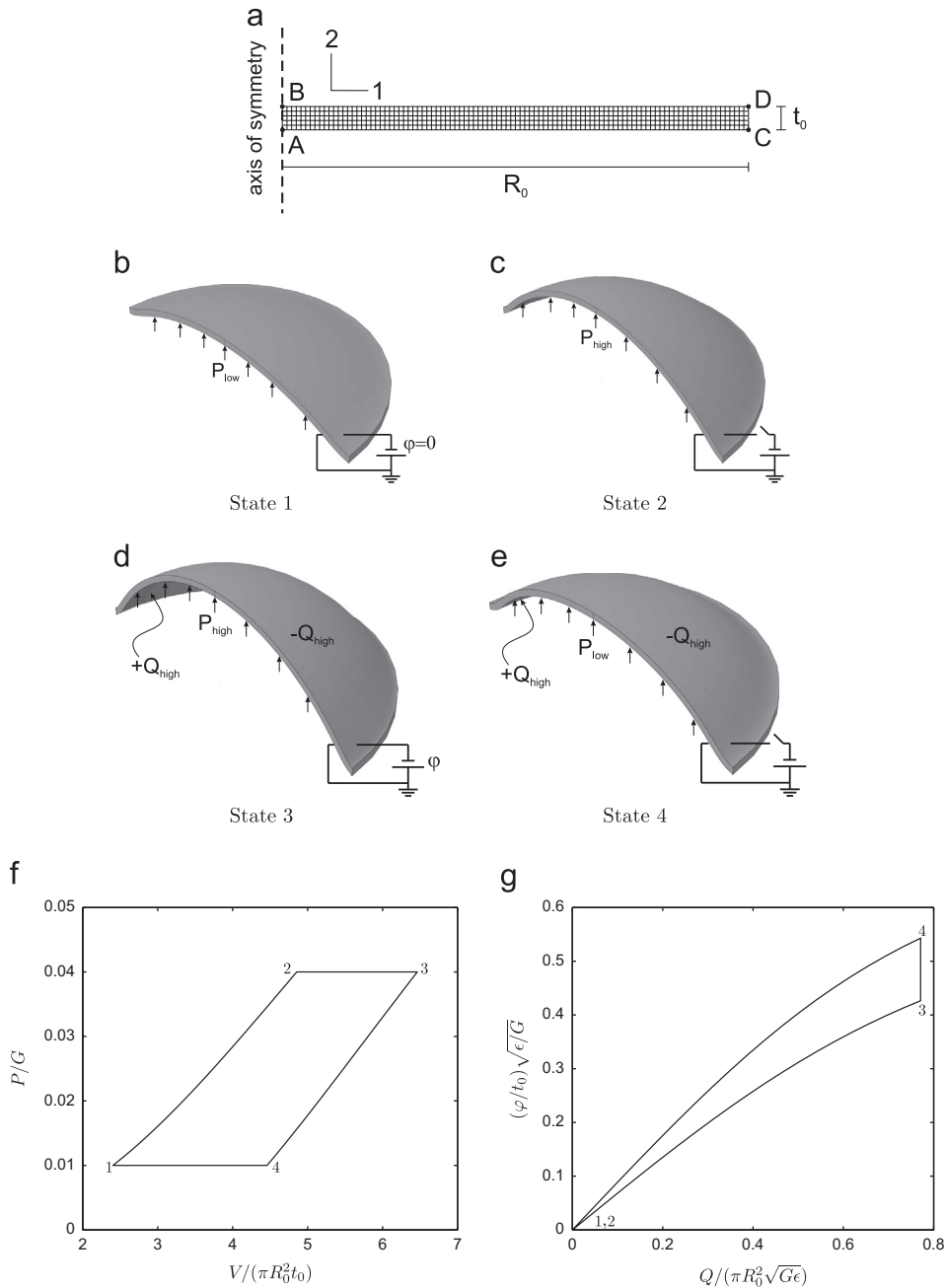


Fig. 7. (a) Initial axisymmetric finite-element mesh for a diaphragm-type energy harvesting device. (b)–(e) The deformed configuration for the four states of the energy harvesting cycle. Half of the diaphragm is visualized for clarity. (f) Pressure–volume and (g) electric potential–charge diagrams for the cycle with the four states labeled.

potential $(\phi/t_0)\sqrt{\epsilon/G}$ and a normalized charge $Q/(\pi R_0^2 \sqrt{G\epsilon})$. We take $P_{high}/G = 0.04$, $P_{low}/P_{high} = 0.25$, and $Q_{high}/(\pi R_0^2 \sqrt{G\epsilon}) = 0.7712$. The mechanical and electrical variables are plotted against each other in Fig. 7(f) and (g), respectively. The four states are labeled on each diagram. The pressure–volume cycle is traversed in a clockwise manner, indicating that mechanical work is expended over the cycle. Conversely, the electric potential–charge diagram is traversed counterclockwise, indicating that electrical energy is harvested. Of importance again is the step 3–4, which involves mechanical unloading at fixed charge. It is this step that raises the electric potential and allows electrical energy to be harvested. From Fig. 7(f) and (g), we determine the amount of energy transformed to be $W = 0.0530G(\pi R_0^2 t_0)$.

Finally, the effect of the process loading parameters P_{low} , P_{high} , and Q_{high} on the transformed energy per cycle is summarized in Fig. 8. The normalized energy transformed per cycle $W/(\pi R_0^2 t_0 G)$ is plotted as a function of the maximum pressure P_{high}/G for maximum charge $Q_{high}/(\pi R_0^2 \sqrt{G\epsilon}) = 0.5, 0.75, 1.0$ and pressure ratios (a) $P_{low}/P_{high} = 0.25$ and (b)

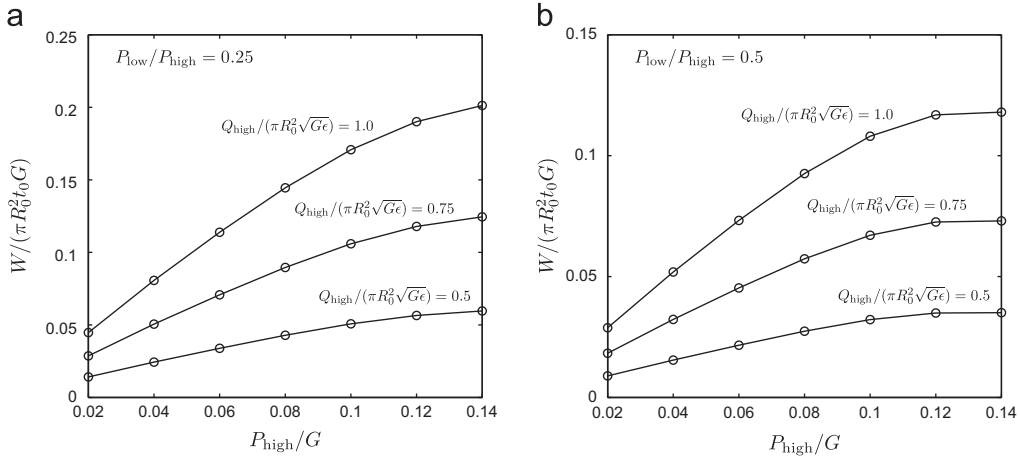


Fig. 8. Normalized energy transformed $W/(\pi R_0^2 t_0 G)$ as a function of the maximum pressure P_{high}/G and maximum charge $Q_{\text{high}}/(\pi R_0^2 \sqrt{G\epsilon})$ for pressure ratios (a) $P_{\text{low}}/P_{\text{high}} = 0.25$ and (b) $P_{\text{low}}/P_{\text{high}} = 0.5$ for the diaphragm-type energy harvesting device.

$P_{\text{low}}/P_{\text{high}} = 0.5$. Again, we observe that higher amounts of energy are transformed for higher maximum charge and lower pressure ratios. (Note the different vertical axis scale bars in Fig. 8(a) and (b)). In this case for the maximum pressure range considered, the transformed energy increases monotonically with increasing P_{high} . A optimal maximum pressure, arising due to chain-locking, analogous to that observed in the barrel-type device, is possible, but greater values of P_{high} were not considered due to mesh distortion.

6. Concluding remarks

In this work, we have formulated a constitutive theory for dielectric elastomers from a thermodynamic viewpoint and have proposed a robust finite-element formulation for the resulting field equations. We have implemented a family of finite elements, including an eight-noded continuum brick, a four-noded axisymmetric element and a four-noded plane-strain element, in the commercial finite-element program Abaqus/Standard by writing user-element subroutines (UELs), and the elements have been verified against analytical results for one-dimensional actuation. We have demonstrated our finite-element capability in each setting: a three-dimensional torsional actuator, a plane-strain bilayer bending actuator and two axisymmetric energy harvesting devices, and shown that we can address design challenges that would be impossible analytically. The user-element subroutines as well as representative Abaqus input files for each application are available online as supplementary material.

This work opens the door for further simulation-based study of complex dielectric elastomeric structures and serves as platform for studying dielectric-elastomer-based composites (Zhang et al., 2002; deBotton et al., 2007; Bertoldi and Gei, 2011; Ponte Castañeda and Siboni, 2012), dissipative effects (Zhao et al., 2011), and instabilities such as wrinkling and creasing of thin, constrained layers (Huang, 2005; Dorfmann and Ogden, 2010; Wang et al., 2011a,b). In particular, interest has grown in structured dielectric elastomers with properties that may be tuned by the application of an electric field (Gei et al., 2011; Shmuel and deBotton, 2012). For example, certain microstructures exhibit band gaps for elastic waves. These band gaps are ranges of frequencies at which elastic waves cannot propagate and may be manipulated by the application of an electric field. The present work will enable the study of complex microstructures made from dielectric elastomers with tunable properties, which would otherwise be intractable to address analytically.

Acknowledgements

D.L.H. and K.B. thank Jay Sayre and Mark Stasik for helpful discussions. This research is funded by Battelle National Security Global Business.

Appendix A. Fringe effects

In this appendix, we examine the effect of the surrounding space on a thin dielectric elastomeric layer sandwiched between two electrodes. This configuration is often used in applications, and it is also investigated in this work, cf. Sections 5.2–5.5. As a representative example, we consider a thin disk of dielectric elastomer with initial radius R_0 and thickness t_0 , such that $t_0 \ll R_0$, subjected to an electric potential difference of φ across the thickness. From straightforward scaling considerations, we can infer that the electric fields in the dielectric elastomer and the surroundings away from the edges of the electrodes scale as φ/t_0 and φ/R_0 , respectively. Furthermore, from (4.5), we infer that the stress and electric displacement in the surroundings scale as $\epsilon_{\text{surr}}(\varphi/R_0)^2$ and $\epsilon_{\text{surr}}\varphi/R_0$, respectively, where ϵ_{surr} is the permittivity of the

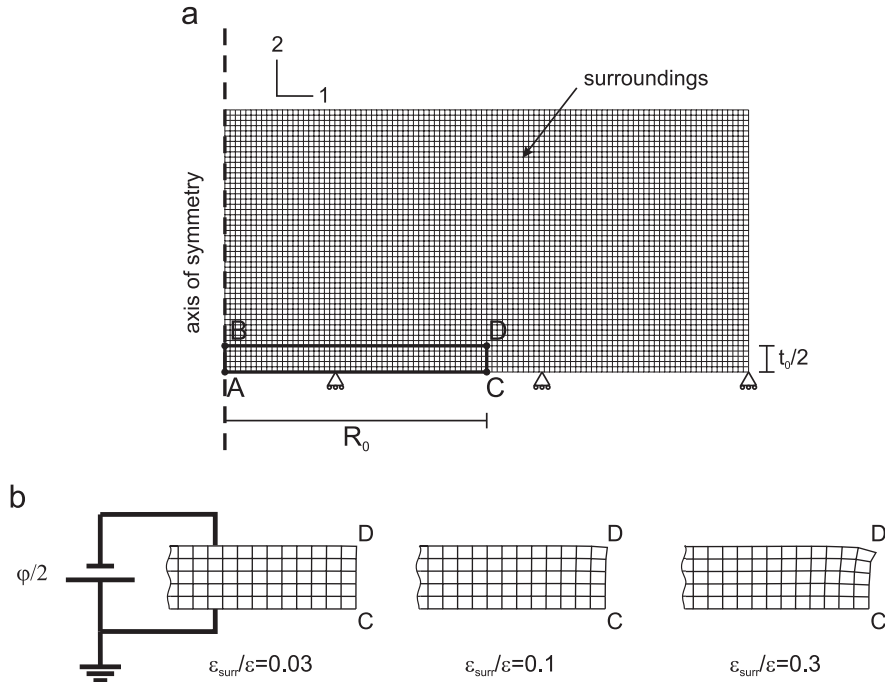


Fig. 9. (a) Initial axisymmetric finite-element mesh for a thin disk of dielectric elastomer and its surroundings. (b) Close-up of the edge of the disk for $(\varphi/t_0)\sqrt{\epsilon/G} = 0.5$ and three permittivity ratios, $\epsilon_{\text{surr}}/\epsilon = 0.03, 0.1, 0.3$.

surroundings. Similarly, the electrostatic stress and electric displacement in the dielectric elastomer away from the boundaries scales as $\epsilon(\varphi/t_0)^2$ and $\epsilon\varphi/t_0$, respectively. Thus, the ratios of the electrostatic stress and electric displacement in the surroundings to that in the dielectric elastomer are $(\epsilon_{\text{surr}}/\epsilon)(t_0/R_0)^2$ and $(\epsilon_{\text{surr}}/\epsilon)(t_0/R_0)$, respectively. When these quantities are small, which is true for the thin dielectric structures considered in Sections 5.2–5.5, neglecting the surroundings has virtually no effect for regions away from the boundaries of the electrodes. However, near the edges of the electrodes, the surroundings can still have an effect, referred to as fringe effects.

Here, we estimate the error introduced by neglecting the surroundings by simulating a dielectric elastomeric actuator in the geometry described above along with its surroundings. The initial axisymmetric finite-element configuration for a disk with $R_0/t_0 = 5$ and its surroundings is shown in Fig. 9(a) with the dielectric elastomer denoted by the region ACDB. The nodes along side AB are set to have $u_1 = 0$, and the nodes along the symmetry plane AC are set to $u_2 = 0$. The side AC is also set to ground with an electric potential of zero, and side BD is constrained such that all nodes along that side have the same electric potential. With this configuration, we are able to solve equilibrium and Gauss's law in the expanded domain. The shear modulus of the surroundings is taken to be six orders of magnitude less than that of the elastomer to approximate a fluid or void, and we consider three permittivity ratios, $\epsilon_{\text{surr}}/\epsilon = 0.03, 0.1, 0.3$. As expected, the actuation response in the interior of the disk for all three cases is indistinguishable from the homogeneous case, cf. (B.4), but a deviation from this response arises near the edge. The edge of the disk at $(\varphi/t_0)\sqrt{\epsilon/G} = 0.5$ is shown in Fig. 9(b) for all three permittivity ratios. For the smallest ratio, the effect is minimal, and as the permittivity of the surroundings is increased relative to that of the elastomer, the effect is increased. From these simulations, we estimate that the error in the calculated displacements introduced by ignoring these effects is no greater than 10% and typically much less for the loading conditions and material properties considered and is localized to a small region $\sim t_0$ from the edge.

Appendix B. Analytical solutions

Here we derive analytical expressions for the applied electric potential versus deformation for one-dimensional actuation of a dielectric elastomer comprised of a Gent material. We assume incompressibility for our analytical computations and then compare the resulting expressions to our simulations for the *nearly* incompressible case. We consider two versions of one-dimensional actuation: axisymmetric and plane-strain.

B.1. Axisymmetric actuation

We begin with the case of axisymmetric, one-dimensional actuation. We consider a cube of material with side length l_0 in the initial configuration, pictured in Fig. 1(a). The displacements of the cube are constrained to be homogeneous with principal stretches $\lambda_1 = \lambda_2 = \lambda > 1$ and $\lambda_3 = 1/\lambda^2$, such that the motion is constant volume, $J = 1$, cf. Fig. 1(b). Moreover, the electric potential on face ABCD is held at zero, while the electric potential on face EFGH is ramped to a value of φ . Under the

assumption of incompressibility, the expression for the Cauchy stress (3.20)₃ becomes

$$\mathbf{T} = G \left(1 - \frac{(\text{tr} \mathbf{B}) - 3}{I_m} \right)^{-1} \mathbf{B} + \epsilon \mathbf{E} \otimes \mathbf{E} - p \mathbf{1}, \quad (\text{B.1})$$

where p is an indeterminate pressure determined by the boundary conditions.

Under the aforementioned set of assumptions, we have

$$[\mathbf{B}] = \begin{bmatrix} \lambda^2 & 0 & 0 \\ 0 & \lambda^2 & 0 \\ 0 & 0 & 1/\lambda^4 \end{bmatrix} \quad \text{and} \quad [\mathbf{E}] = \begin{bmatrix} 0 \\ 0 \\ \lambda^2 \left(\frac{\varphi}{l_0} \right) \end{bmatrix}. \quad (\text{B.2})$$

Since the Cauchy stress is zero in all components, we have

$$\begin{aligned} G \left(1 - \frac{2\lambda^2 + (1/\lambda^4) - 3}{I_m} \right)^{-1} \lambda^2 - p &= 0, \\ G \left(1 - \frac{2\lambda^2 + (1/\lambda^4) - 3}{I_m} \right)^{-1} \left(\frac{1}{\lambda^4} \right) + \epsilon \lambda^4 \left(\frac{\varphi}{l_0} \right)^2 - p &= 0. \end{aligned} \quad (\text{B.3})$$

Eliminating p in (B.3) and rearranging, we arrive at the following expression:

$$\frac{\varphi}{l_0} \sqrt{\frac{\epsilon}{G}} = \sqrt{\left(1 - \frac{2\lambda^2 + (1/\lambda^4) - 3}{I_m} \right)^{-1} \frac{1}{\lambda^2} \left(1 - \frac{1}{\lambda^6} \right)}. \quad (\text{B.4})$$

We note that for the Neo-Hookean case, where $I_m \rightarrow \infty$, (B.4) becomes

$$\frac{\varphi}{l_0} \sqrt{\frac{\epsilon}{G}} = \frac{1}{\lambda} \sqrt{\left(1 - \frac{1}{\lambda^6} \right)}. \quad (\text{B.5})$$

B.2. Plane-strain

For the case of incompressible, plane-strain, one-dimensional actuation, we consider a deformation with principal stretches $\lambda_1 = 1$, $\lambda_2 = \lambda > 1$ and $\lambda_3 = 1/\lambda$, cf. Fig. 1(c), such that

$$[\mathbf{B}] = \begin{bmatrix} 1 & 0 & 0 \\ 0 & \lambda^2 & 0 \\ 0 & 0 & 1/\lambda^2 \end{bmatrix} \quad \text{and} \quad [\mathbf{E}] = \begin{bmatrix} 0 \\ 0 \\ \lambda \left(\frac{\varphi}{l_0} \right) \end{bmatrix}. \quad (\text{B.6})$$

Next, applying the condition that the normal components of the Cauchy stress in the two- and three-directions are zero, we have

$$\begin{aligned} G \left(1 - \frac{\lambda^2 + (1/\lambda^2) - 2}{I_m} \right)^{-1} \lambda^2 - p &= 0, \\ G \left(1 - \frac{\lambda^2 + (1/\lambda^2) - 2}{I_m} \right)^{-1} \left(\frac{1}{\lambda^2} \right) + \epsilon \lambda^2 \left(\frac{\varphi}{l_0} \right)^2 - p &= 0. \end{aligned} \quad (\text{B.7})$$

Eliminating p in (B.7) and rearranging, we obtain the following expression relating the lateral stretch λ to the dimensionless electric potential:

$$\frac{\varphi}{l_0} \sqrt{\frac{\epsilon}{G}} = \sqrt{\left(1 - \frac{\lambda^2 + (1/\lambda^2) - 2}{I_m} \right)^{-1} \left(1 - \frac{1}{\lambda^4} \right)}. \quad (\text{B.8})$$

Finally, in the Neo-Hookean case, when $I_m \rightarrow \infty$, we have

$$\frac{\varphi}{l_0} \sqrt{\frac{\epsilon}{G}} = \sqrt{\left(1 - \frac{1}{\lambda^4} \right)}. \quad (\text{B.9})$$

Appendix C. Supplementary data

Supplementary data associated with this article can be found in the online version at <http://dx.doi.org/10.1016/j.jmps.2013.05.003>.

References

- Abaqus/Standard, 2010. Reference Manuals.
- Bar-Cohen, Y. (Ed.), 2001. Electroactive Polymer (EAP) Actuators as Artificial Muscles. SPIE Press, Bellingham, WA.
- Bertoldi, K., Gei, M., 2011. Instabilities in multilayered soft dielectrics. *J. Mech. Phys. Solids* 59, 18–42.
- Brochu, P., Pei, Q., 2010. Advances in dielectric elastomers for actuators and artificial muscles. *Macromol. Rapid Commun.* 31, 10–36.
- Bustamante, R., Dorfmann, A., Ogden, R.W., 2009. Nonlinear electroelastostatics: a variational framework. *Z. Angew. Math. Phys.* 60, 154–177.
- Carpi, F., Migliore, A., Serra, G., De Rossi, D., 2005. Helical dielectric elastomer actuators. *Smart Mater. Struct.* 14, 1210–1216.
- Carpi, F., Smela, E. (Eds.), 2009. Biomedical Applications of Electroactive Polymer Actuators. John Wiley and Sons, Chichester, UK.
- Carpi, F., de Rossi, D., Kornbluh, R., Pelrine, R., Sommer-Larsen, P. (Eds.), 2008. Dielectric Elastomers as Electromechanical Transducers. Elsevier, Oxford, UK.
- Chester, S.A., Anand, L., 2011. A thermo-mechanically coupled theory for fluid permeation in elastomeric materials: application to thermally responsive gels. *J. Mech. Phys. Solids* 59, 1978–2006.
- deBotton, G., Tevet-Deree, L., Socolsky, E.A., 2007. Electroactive heterogeneous polymers: analysis and applications to laminated composites. *Mech. Adv. Mater. Struct.* 14, 13–22.
- de Souza Neto, E.A., Perić, D., Dutko, M., Owen, D.R.J., 1996. Design of simple low order finite elements for large strain analysis of nearly incompressible solids. *Int. J. Solids Struct.* 33, 3277–3296.
- Dorfmann, A., Ogden, R.W., 2005. Nonlinear electroelasticity. *Acta Mech.* 174, 167–183.
- Dorfmann, A., Ogden, R.W., 2010. Nonlinear electroelastostatics: incremental equations and stability. *Int. J. Eng. Sci.* 48, 1–14.
- Eringen, A.C., Maugin, G.A., 1990. *Electrodynamics of Continua*, vol. I. Springer, New York.
- Gao, Z., Tuncer, A., Cuitiño, A.M., 2011. Modeling and simulation of the coupled mechanical–electrical response of soft solids. *Int. J. Plast.* 27, 1459–1470.
- Gei, M., Roccabianca, S., Bacca, M., 2011. Controlling bandgap in electroactive polymer-based structures. *IEEE/ASME Trans. Mech.* 16, 102–107.
- Gent, A.N., 1996. A new constitutive relation for rubber. *Rubber Chem. Technol.* 69, 59–61.
- Goulbourne, N., Mockensturm, E., Frecker, M., 2005. A nonlinear model for dielectric elastomer membranes. *J. Appl. Mech.* 72, 899–906.
- Hossain, M., Vu, D.K., Steinmann, P., 2012. Experimental study and numerical modelling of VHB 4910 polymer. *Comput. Mater. Sci.* 59, 65–74.
- Huang, R., 2005. Electrically induced surface instability of a conductive thin film on a dielectric substrate. *Appl. Phys. Lett.* 87, 151911.
- Kornbluh, R.D., Pelrine, R., Pei, Q., Oh, S., Joseph, J., 2000. Ultrahigh strain response of field-actuated elastomeric polymers. *Proc. SPIE* 3987, 51–64.
- Kornbluh, R.D., Pelrine, R., Prahlad, H., Wong-Foy, A., McCoy, B., Kim, S., Eckerle, J., Low, T., 2011. From boots to buoys: promises and challenges of dielectric elastomer energy harvesting. *Proc. SPIE* 7976, 797605.
- Kornbluh, R.D., Pelrine, R., Prahlad, H., Wong-Foy, A., McCoy, B., Kim, S., Eckerle, J., Low, T., 2012. Dielectric elastomers: stretching the capabilities of energy harvesting. *MRS Bull.* 37, 246–253.
- Maugin, G.A., 1980. The method of virtual power in continuum mechanics: application to coupled fields. *Acta Mech.* 35, 1–70.
- Maugin, G.A., 1988. *Continuum Mechanics of Electromagnetic Solids*. North Holland, Amsterdam, The Netherlands.
- Maugin, G.A., Pouget, J., Drouot, R., Collet, B., 1992. Nonlinear Electromechanical Couplings. John Wiley and Sons, Chichester, UK.
- McMeeking, R.M., Landis, C.M., 2005. Electrostatic forces and stored energy for deformable dielectric materials. *J. Appl. Mech.* 72, 581–590.
- McMeeking, R.M., Landis, C.M., Jimenez, S.M.A., 2007. A principle of virtual work for combined electrostatic and mechanical loading of materials. *Int. J. Non-Linear Mech.* 42, 831–838.
- Park, H.S., Suo, Z., Zhou, J., Klein, P.A., 2012. A dynamic finite element method for inhomogeneous deformation and electromechanical instability of dielectric elastomer transducers. *Int. J. Solids Struct.* 49, 2187–2194.
- Pelrine, R.E., Kornbluh, R.D., Joseph, J.P., 1998. Electrostriction of polymer dielectrics with compliant electrodes as a means of actuation. *Sens. Actuators A* 64, 77–85.
- Pelrine, R., Kornbluh, R., Joseph, J., Heydt, R., Pei, Q., Chiba, S., 2000a. High-field deformation of elastomeric dielectrics for actuators. *Mater. Sci. Eng. C* 11, 89–100.
- Pelrine, R., Kornbluh, R., Pei, Q., Joseph, J., 2000b. High-speed electrically actuated elastomers with strain greater than 100%. *Science* 287, 836–839.
- Plante, J.-S., Dubowsky, S., 2006. Large-scale failure modes of dielectric elastomer actuators. *Int. J. Solids Struct.* 43, 7727–7751.
- Ponte Castañeda, P., Siboni, M.H., 2012. A finite-strain constitutive theory for electro-active polymer composites via homogenization. *Int. J. Non-Linear Mech.* 47, 293–306.
- Rudykh, S., deBotton, G., 2012. Instabilities of hyperelastic fiber composites: micromechanical versus numerical analyses. *J. Elast.* 106, 123–147.
- Shmuel, G., deBotton, G., 2012. Band-gaps in electrostatically controlled dielectric laminates subjected to incremental shear motions. *J. Mech. Phys. Solids* 60, 1970–1981.
- Suo, Z., Zhao, X., Greene, W.H., 2008. A nonlinear field theory of deformable dielectrics. *J. Mech. Phys. Solids* 56, 467–486.
- Tagarielli, V.L., Hildick-Smith, R., Huber, J.E., 2012. Electro-mechanical properties and electrostriction response of a rubbery polymer for EAP applications. *Int. J. Solids Struct.* 49, 3409–3415.
- Toupin, R.A., 1956. The elastic dielectric. *J. Ration. Mech. Anal.* 5, 849–915.
- Toupin, R.A., 1963. A dynamical theory of elastic dielectrics. *Int. J. Eng. Sci.* 1, 101–126.
- Vu, D.K., Steinmann, P., 2007. Theoretical and numerical aspects of the material and spatial settings in nonlinear electro-elastostatics. *Int. J. Frac.* 147, 109–116.
- Vu, D.K., Steinmann, P., Possart, G., 2007. Numerical modelling of non-linear electroelasticity. *Int. J. Numer. Methods Eng.* 70, 685–704.
- Wang, Q., Tahir, M., Zhang, L., Zhao, X., 2011. Electro-creasing instability in deformed polymers: experiment and theory. *Soft Matter* 7, 6583–6589.
- Wang, Q., Zhang, L., Zhao, X., 2011. Creasing to cratering instability in polymers under ultrahigh electric fields. *Phys. Rev. Lett.* 106, 118301.
- Wissler, M., Mazza, E., 2005. Modeling and simulation of dielectric elastomer actuators. *Smart Mater. Struct.* 14, 1396–1402.
- Wissler, M., Mazza, E., 2007. Mechanical behavior of an acrylic elastomer used in dielectric elastomer actuators. *Sens. Actuators A* 134, 494–504.
- Zhang, Q.M., Bharti, V., Zhao, X., 1998. Giant electrostriction and relaxor ferroelectric behavior in electron-irradiated poly(vinylidene fluoride-trifluoroethylene) copolymer. *Science* 280, 2101–2104.
- Zhang, Q.M., Li, H., Poh, M., Xia, F., Cheng, Z.-Y., Xu, H., Huang, C., 2002. An all-organic composite actuator material with a high dielectric constant. *Nature* 419, 284–287.
- Zhao, X., Hong, W., Suo, Z., 2007. Electromechanical hysteresis and coexistent states in dielectric elastomers. *Phys. Rev. B* 76, 134113.
- Zhao, X., Suo, Z., 2008a. Electrostriction in elastic dielectrics undergoing large deformation. *J. Appl. Phys.* 104, 123530.
- Zhao, X., Suo, Z., 2008b. Method to analyze programmable deformation of dielectric elastomer layers. *Appl. Phys. Lett.* 93, 251902.
- Zhao, X., Koh, S.J.A., Suo, Z., 2011. Nonequilibrium thermodynamics of dielectric elastomers. *Int. J. Appl. Mech.* 3, 203–217.
- Zhou, J., Hong, W., Zhao, X., Zhang, Z., Suo, Z., 2008. Propagation of instability in dielectric elastomers. *Int. J. Solids Struct.* 45, 3739–3750.